TUDelft

Delft University of Technology

Investigation of dynamic wind loads on a long-span suspension bridge identified from measured acceleration data

Petersen, W.; Øiseth, O.; Lourens, E.

Investigation of dynamic wind loads on a long-span suspension bridge identified from measured acceleration data

Ø.W. Petersen [a,*], O. Øiseth [a], E. Lourens [b]

[a] *NTNU, Norwegian University of Science and Technology, 7491, Trondheim, Norway*
[b] *Delft University of Technology, 2628, CN, Delft, the Netherlands*

ARTICLE INFO

ABSTRACT

The traditional wind load assessment for long-span bridges relies on assumed models for the wind field and aerodynamic coefficients from wind tunnel tests, which usually introduce some uncertainties. Recent studies have shown that large deviations can exist between the predicted and observed wind-induced dynamic response of suspension bridges. In studies of the dynamical behavior of bridges, inverse force identification methods can therefore be an interesting tool in the assessment of possible uncertainties involved in the modeling of wind loads. This paper presents a novel case study of the identification of the dynamic wind loads on the 1310 m long Hardanger bridge, a suspension bridge equipped with a monitoring system for wind and vibrations. The modal wind loads are identified from acceleration data using an algorithm for model-based joint input and state estimation. Several data sets with different wind conditions are presented. The wind loads are studied in the time and frequency domains and are compared to the mean velocity and turbulence characteristics of the wind.

1. Introduction

As the development of bridges has led to longer and more slender spans, the assessment of wind loads has become increasingly critical for reliable structural design (Larsen and Larose, 2015). Modern wind load and response analysis is based mostly on theories of buffeting due to turbulence (Scanlan, 1978a) and self-excitation due to bridge motion (Scanlan, 1978b) that have been refined in a variety of formulations: comparisons can be found in (Chen and Kareem, 2002; Kavrakov and Morgenthal, 2017). Although these theories are well established, the actual parameters that go into this analysis can be a significant source of uncertainty (Jakobsen and Tanaka, 2003; Caracoglia, 2008). The classic wind load assessment also relies on aerodynamic coefficients and admittance functions for the specific bridge geometry that are usually obtained from wind tunnel tests using scale models. Simplifications and uncertainties from these tests transfer directly to the predicted wind loads. Although the computational methodology and technology for wind tunnel testing have become sophisticated (Siedziako et al., 2017; Diana et al., 2004; Cigada et al., 2001), the local conditions and complexity experienced by an actual bridge cannot be recreated. For instance, the lack of case-specific data usually leads to several simplified

assumptions: the wind field is stationary, homogeneous, and normal to the bridge. These assumptions neglect phenomena that can occur in reality: non-stationary events, an inhomogeneous or skew wind field, and the influence of local topology. Some full-scale studies also report discrepancies between the predicted and measured responses of long-span bridges (Fenerci and Øiseth, 2017; Wang et al., 2012; Macdonald, 2003; Bietry et al., 1995; Cheynet et al., 2016), indicating that there are still some uncertainty gaps for predicted wind loading.

The real wind loads on large structures cannot be measured directly in a practical manner. An alternative approach to this problem is the inverse estimation of loads from response data, also known as force identification. These techniques require (limited) measured vibration data and a finite element (FE) model of the structure. A well-known challenge in inverse force identification is issues related to the problem of ill-posedness (Jacquelin et al., 2003; Lourens, 2012), meaning that the solution is generally sensitive to numerical errors, measurement noise, and model errors, which are inevitably present in non-synthetic data. In recent years, many different techniques for force identification have been proposed. Furthermore, various Kalman-type filters (Ma et al., 2003; Azam et al., 2015; Lourens et al., 2012a, 2012b; Maes et al., 2018; Song, 2018) and frequency-domain (Liu and Shepard, 2005; Rezayat et al.,

---

* Corresponding author.
E-mail addresses: oyvind.w.petersen@ntnu.no (Ø.W. Petersen), ole.oiseth@ntnu.no (O. Øiseth), e.lourens@tudelft.nl (E. Lourens).
URL: https://www.ntnu.edu/kt/research/dynamics (Ø.W. Petersen).

2016) and time-domain (Li et al., 2015; Qiao et al., 2016; Aucejo et al., 2018a; Sun et al., 2015; Lai et al., 2017; Chang et al., 2019; Bernal and Ussia, 2015) deconvolution approaches with regularization schemes have been investigated.

Inverse estimation of wind loads on tall buildings has been studied in wind tunnels (Zhi et al., 2018; Hwang et al., 2011) and in full-scale conditions (Zhi et al., 2016; Kang et al., 2012; Niu et al., 2015). Reconstruction of wind loads on small-scale guyed masts have also been reported (Amiri and Bucher, 2017). While an increasing number of cable-supported bridges are equipped with data monitoring systems (Ko and Ni, 2005; Wong, 2004), to the best of the authors' knowledge, no studies have focused on the inverse estimation of wind loads. Therefore, it is of interest to test the state-of-the-art force identification methodologies with full-scale data and to assess their utility as a tool in detailed studies of wind loads. As will be explained, force identification does not utilize any specific load model assumptions, which makes the methodology attractive for studies of non-stationary data, wind gusts or abnormal events, and could help to provide a better understanding of the mechanisms behind wind loads. Before such detailed studies can be performed, the performance of the methods must be evaluated to identify the weak and strong points. Although the inverse methods have been explored in laboratory experiments, the transition to full-scale bridges means that different conditions and uncertainties will play an important role.

In this article, the dynamic wind loads on the Hardanger bridge are estimated based on acceleration data. The capability of the full-field estimation of these algorithms for long-span bridges was studied previous works (Petersen and Øiseth, 2019), showing that the methodology is feasible, with the main limitation being the number of modal responses that can be reconstructed.

The rest of this paper is organized as follows. Section 2 presents the bridge case study and the methodology. In Section 3, results from several data sets with different wind conditions are examined. The loads are assessed in the time and frequency domains, and the influence of the wind characteristics on the loads are investigated. A short discussion of the usefulness of the methodology is provided, and conclusions are given in Section 4.

2. Case study: the Hardanger bridge

2.1. The bridge and monitoring system

The Hardanger bridge (Fig. 1) is a suspension bridge with a main span of 1310 m. Crossing the Hardanger fjord, the bridge is located in a fjord-mountainous terrain (Fig. 2). The long-span and slender features of the bridge make it sensitive to excitations from wind approaching from the coastal area to the west or the inland mountainous regions to the east. The bridge is a valuable case study for future long and slender bridges planned for similarly complex terrains, and a structural monitoring system has been in operation since 2013. Fig. 3 shows the positions of the

Fig. 1. View of the Hardanger bridge from the north end (Photo: Øyvind Wiig Petersen/NTNU).
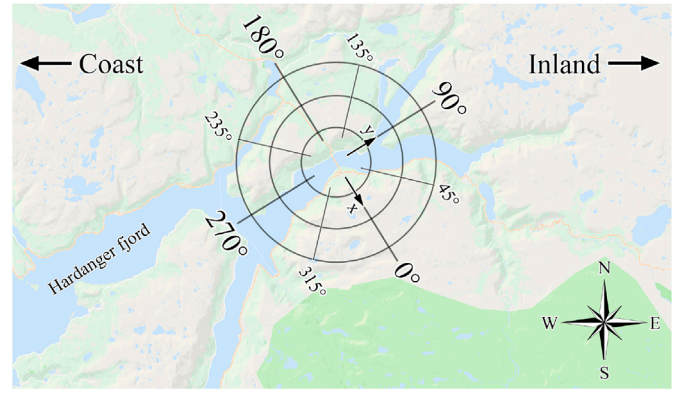

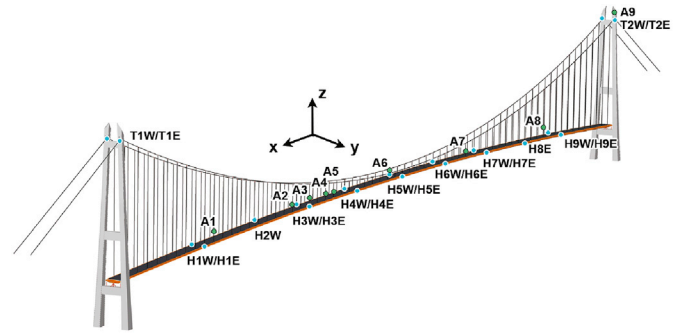Fig. 2. Topography of the area surrounding the bridge.

Fig. 3. Positions of the sensors on the Hardanger bridge.

installed sensors. Eight digital ultrasonic anemometers A1-A8 (Gill Wind Master Pro 3D) are mounted on the hangers along the bridge span. Twenty triaxial accelerometers (CUSP-3D strong-motion, range $\pm$ 4 g, SNR 130 dB) are located in the girder and the towers. More detailed specifications of this system are given in (Fenerci et al., 2017).

2.2. Equations for bridge dynamics in force identification framework

In the following, a short derivation of the state-space equations for the dynamic system modeling is provided. These equations for reduced-order multimodal systems are fairly well known but are included here for a clear problem definition. For studies of wind-induced response in regular in-operation conditions, a linear dynamic model is adequate, and the equations of motion for the bridge in a FE format can be given by:

$$\mathbf{M}_0\ddot{\mathbf{u}}(t) + \mathbf{C}_0\dot{\mathbf{u}}(t) + \mathbf{K}_0\mathbf{u}(t) = \mathbf{f}(t) \tag{1}$$

where the subscript $(\cdot)_0$ denotes the still-air properties, i.e., contribution from the structure only. The vector $\mathbf{u}(t) \in \mathbb{R}^{n_{DOF}}$ is the response of the physical DOF, and $\mathbf{f}(t) \in \mathbb{R}^{n_{DOF}}$ a force vector. To reduce the model order, the reduction basis is constructed from a set of n_m mass-normalized still-air vibration modes $\boldsymbol{\varphi}_j \in \mathbb{R}^{n_{DOF}}$:

$$\left(\mathbf{K}_0 - \omega_j^2\mathbf{M}_0\right)\boldsymbol{\varphi}_j = \mathbf{0} \tag{2}$$

Further, the full response is approximated by $\mathbf{u}(t) \approx \boldsymbol{\Phi}\mathbf{z}(t)$, where $\boldsymbol{\Phi} = [\boldsymbol{\varphi}_1\ \boldsymbol{\varphi}_2...\boldsymbol{\varphi}_{n_m}] \in \mathbb{R}^{n_{DOF}\times n_m}$ and $\mathbf{z}(t) \in \mathbb{R}^{n_{DOF}}$ is the generalized coordinate vector. Assuming the damping matrix $\mathbf{C}_0$ is proportional, the generalized equation of motion becomes:

$$\ddot{\mathbf{z}}(t) + 2\boldsymbol{\Xi}\boldsymbol{\Omega}\dot{\mathbf{z}}(t) + \boldsymbol{\Omega}^2\mathbf{z}(t) = \boldsymbol{\Phi}^{\mathrm{T}}\mathbf{f}(t) = \mathbf{p}(t) \tag{3}$$

where $\boldsymbol{\Omega} = \mathrm{diag}(\omega_1, ..., \omega_{n_m})$ and $\boldsymbol{\Xi} = \mathrm{diag}(\xi_1, ..., \xi_{n_m})$ are diagonal matrices assigned the still-air natural frequencies ($\omega_j = 2\pi f_j$) and

damping ratios. The measurement vector $\mathbf{y}(t) \in \mathbb{R}^{n_y}$, which consists of accelerations and displacements in selected structural DOFs, is given as follows:

$$\mathbf{y}(t) = \mathbf{S}_a \ddot{\mathbf{u}}(t) + \mathbf{S}_d \mathbf{u}(t) \tag{4}$$

where $\mathbf{S}_a$ and $\mathbf{S}_d \in \mathbb{R}^{n_d \times n_{DOF}}$ are binary matrices that select the measured DOFs. By introducing the modal state variable $\mathbf{x}(t) = [\mathbf{z}(t)^T \quad \dot{\mathbf{z}}(t)^T]^T \in \mathbb{R}^{2n_m}$, the system equations is converted into state-space form:

$$\dot{\mathbf{x}}(t) = \mathbf{A}_c \mathbf{x}(t) + \mathbf{B}_c \mathbf{p}(t) \tag{5}$$

$$\mathbf{y}(t) = \mathbf{G}_c \mathbf{x}(t) + \mathbf{J}_c \mathbf{p}(t) \tag{6}$$

$$\mathbf{A}_c = \begin{bmatrix} 0 & \mathbf{I} \\ -\mathbf{\Omega}^2 & -2\mathbf{\Xi}\mathbf{\Omega} \end{bmatrix} \tag{7}$$

$$\mathbf{B}_c = \begin{bmatrix} \mathbf{0} \\ \mathbf{I} \end{bmatrix} \tag{8}$$

$$\mathbf{G}_c = [\mathbf{S}_d \mathbf{\Phi} - \mathbf{S}_a \mathbf{\Phi}\mathbf{\Omega}^2 \quad -\mathbf{S}_a \mathbf{\Phi} 2\mathbf{\Omega}\mathbf{\Xi}] \tag{9}$$

$$\mathbf{J}_c = [\mathbf{S}_a \mathbf{\Phi}] \tag{10}$$

In the discretization to an intersample time $\Delta t = 0.1$ s, a first-order hold constraint is imposed on the input. This constraint is necessary to preserve the model accuracy for the very low-frequency range, which is important for analysis of the wind-induced response. After the addition of stochastic noise, this process yields the following model equations:

$$\overline{\mathbf{x}}_{k+1} = \mathbf{A}\overline{\mathbf{x}}_k + \mathbf{B}\mathbf{p}_k + \mathbf{v}_k \tag{11}$$

$$\mathbf{y}_k = \mathbf{G}\overline{\mathbf{x}}_k + \mathbf{J}\mathbf{p}_k + \mathbf{w}_k \tag{12}$$

where the secondary state $\overline{\mathbf{x}}_k = \mathbf{x}_k - \mathbf{F}\mathbf{p}_k$ is introduced (Aucejo et al., 2018b) and the system matrices are given by:

$$\mathbf{A} = \exp(\mathbf{A}_c \Delta t) \tag{13}$$

$$\mathbf{B} = (\mathbf{A} - \mathbf{I})\mathbf{A}_c^{-1}\mathbf{B}_c - \mathbf{F} + \mathbf{A}\mathbf{F} \tag{14}$$

$$\mathbf{F} = (\mathbf{A}_c^{-1}(\mathbf{A} - \mathbf{I}) / \Delta t - \mathbf{I})\mathbf{A}_c^{-1}\mathbf{B}_c \tag{15}$$

$$\mathbf{G} = \mathbf{G}_c \tag{16}$$

$$\mathbf{J} = \mathbf{J}_c + \mathbf{G}_c \mathbf{F} \tag{17}$$

The vectors $\mathbf{w}_k \in \mathbb{R}^{2n_m}$ and $\mathbf{v}_k \in \mathbb{R}^{n_y}$ are zero-mean white noise terms that model the uncertainties of the states and measurements. Their corresponding covariance matrices are given by:

$$\begin{aligned} \mathbb{E}[\mathbf{w}_k \mathbf{w}_l^T] &= \mathbf{Q}\,\delta_{kl} \\ \mathbb{E}[\mathbf{v}_k \mathbf{v}_l^T] &= \mathbf{R}\,\delta_{kl} \\ \mathbb{E}[\mathbf{w}_k \mathbf{v}_l^T] &= \mathbf{S}\,\delta_{kl} \end{aligned} \tag{18}$$

A clear model definition of the unknown forces is essential in the context of input estimation. For cable-supported bridges, the wind forces are not localized to a small number of nodes but are distributed along the entire bridge. The full force vector $\mathbf{f}(t)$ in Eq. (1) takes into account any type of loading that may be present (buffeting forces, self-excited forces, traffic forces, etc.). The system formulation in Eqs. (11) and (12) considers these forces projected to a modal space, i.e., $\mathbf{\Phi}^T \mathbf{f}(t) = \mathbf{p}(t) \in \mathbb{R}^{n_m}$.

In this work, the well-established joint input-state estimation algorithm (JIS) (Lourens et al., 2012b), which can be classified as a Kalman-type technique, is used. This method provides minimum-variance estimates of the states ($\widehat{\overline{\mathbf{x}}}(t_k)$) and input forces ($\widehat{\mathbf{p}}(t_k)$). In addition, a dual Kalman filter (DKF) (Azam et al., 2015) and a time-domain sequential deconvolution method (Bernal and Ussia, 2015) are tested. For more detailed information on the estimation methods, we refer to the cited works.

Contrary to classic (forward) modeling of wind loads, no specific time-space assumptions are imposed on the wind field or the wind forces. Since the force identification is driven directly by the vibration data (and the system model), there is no model for the wind field and no functions are given for the aerodynamic coefficients and admittance of the bridge deck. This is critical since the study is not constrained to cases with idealized load conditions so that one can study loading from wind fields that are skew, inhomogeneous, non-stationary or essentially unknown.

2.3. System model and limitations in the methodology

The still-air modes are solved from a FE model of the bridge (Fig. 4). The model is tuned via a model updating procedure to match modal properties from operational modal analysis; see (Petersen and Øiseth, 2019) for details. Table 1 lists the modes, where the labels H, V, T and P, respectively, denote horizontal, vertical, torsion and pylon motions. The identified (almost) still-air damping ratios $\overline{\xi}_j$ in Table 1 are adopted for the state-space model.

The system model is truncated to contain only 18 modes, a choice explained in the following. In most force identification methods, the number of unknown forces is theoretically limited by the number of linearly independent outputs. The identification of modal forces requires that $\text{rank}(\mathbf{J}) = n_m$ in an instantaneous inversion of system (Maes et al., 2014). Fig. 5 shows the evaluation of the singular values of $\mathbf{J}$ for different model sizes. The clearly visible singular value drop-off for the 19-mode model indicates close-to-linear relationships in the output data, which increases the condition number of this matrix. Therefore, no more than 18 modal forces could be identified without running into severe ill-conditioning in the system inversion. This number of forces is notably less than the upper theoretical limit governed by the aforementioned rank-criterion, highlighting the importance of designing optimal sensor locations, in particular for long-span bridges that have many modes that contribute to the wind-induced total response. The truncated system model accounts for roughly 80% of the measured acceleration data.

Some limitations exist when only acceleration data are available, and the workarounds and effects hereof are discussed in the following. To obtain a steady state of the filter gain matrices and reduce the computational time, displacement data are generated by numerical integration of the accelerations. The influences of these displacements are weighted downward to rely mostly on the acceleration data. In filtering type applications, the covariance matrices are often considered tuning parameters for the system; $\mathbf{R}$ is set to diagonal with values of 10^{-6} for the accelerations and 10^{-2} for the displacements. This process is similar to the principle of using dummy measurements for stabilization, as proposed in (Naets et al., 2015); the displacement outputs are strongly penalized to lessen their influence while maintaining a stable solution. A value of $\mathbf{Q} = 10^{-3}\,\mathbf{I}$ is adopted for the noise on the states. The solution is insensitive to a scaling of these matrices of several orders up or down.

Since the inverse algorithms are linear filters, the frequency content of the estimated forces directly relates to the output data. In the very-low-frequency range, the accelerations are not very sensitive to the modal forces. Although the installed accelerometers perform well for very-low-frequency vibrations, the data below approximately 0.01 Hz could contain errors or be affected by the removal of very small linear trends. The force estimates are therefore high-pass filtered at 0.01 Hz in the post-processing of the results. The actual buffeting loads due to turbulence do, however, have low-frequency components below this limit. Ideally, actual static-sensitive measurement data could be used to obtain better
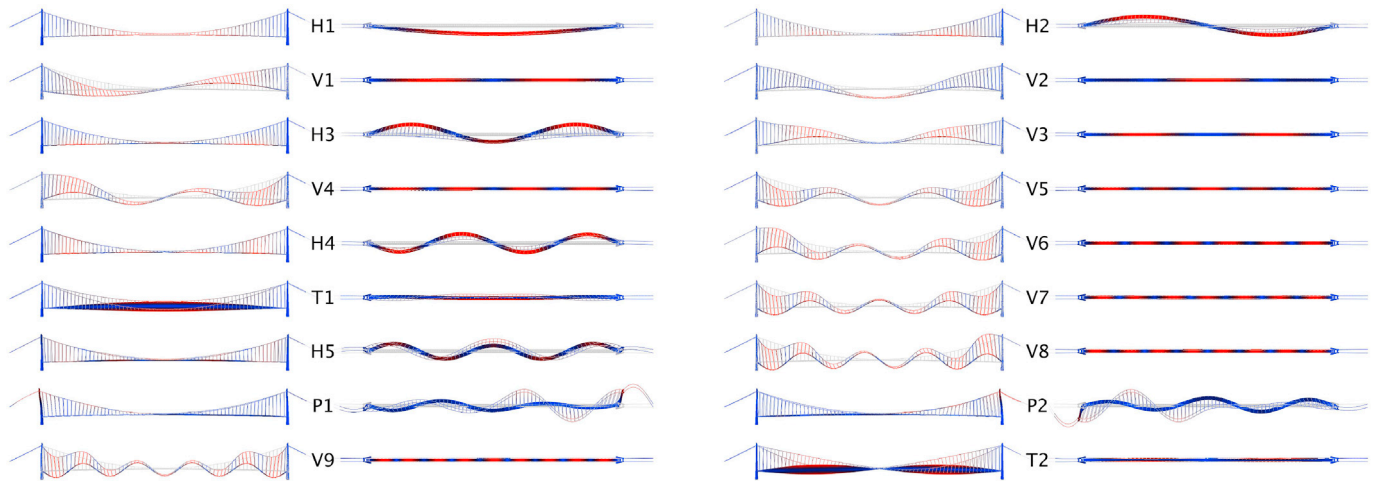
Fig. 4. Still-air modes in the system model.

Table 1

Properties of the still-air modes in the system model. The symbols $\overline{f}_j$, $\overline{\xi}_j$, and $\overline{\varphi}_j$ denote identified modal properties (Petersen and Øiseth, 2019).

Mode no. j	Mode name	f_j [Hz]	$\overline{f}_j$ [Hz]	$\overline{\xi}_j$ [%]	MAC(φ_j, Re($\overline{\varphi}_j$))
1	H1	0.051	0.052	0.65	0.999
2	H2	0.105	0.105	0.77	0.993
3	V1	0.112	0.119	1.77	0.989
4	V2	0.142	0.142	0.65	0.995
5	H3	0.185	0.183	0.77	0.993
6	V3	0.203	0.206	0.27	0.992
7	V4	0.212	0.212	0.35	0.997
8	V5	0.276	0.276	0.26	0.998
9	H4	0.318	0.318	0.63	0.990
10	V6	0.332	0.333	0.25	0.995
11	T1	0.371	0.374	0.41	0.964
12	V7	0.401	0.401	0.24	0.997
13	H5	0.463	0.464	1.56	0.704
14	V8	0.468	0.471	0.26	0.991
15	P1	0.511	0.516	0.16	0.889
16	P2	0.518	0.529	0.22	0.859
17	V9	0.545	0.547	0.31	0.998
18	T2	0.550	0.560	0.65	0.978

Fig. 5. Singular values of **J** for different model sizes.

low-frequency estimates, but such data were unfortunately not available. Furthermore, the purely static forces ($f = 0$ Hz) are theoretically impossible to reconstruct from acceleration data alone (Maes et al., 2014) and are therefore not considered further.

In addition, the output data are low-pass filtered at 0.6 Hz during preprocessing since the contributions above this limit belong to modes not accounted for by the system model (Table 1). In summary, only the dynamic force content in the range $f \in [0.01, 0.6]$ Hz is considered. Different results could be obtained for other bridges or sensor network configurations.

3. Identification of wind loads

3.1. Assessment of load characteristics

The four selected recordings that are used in this study are listed in Table 2. As will be shown, these recordings reflect the variability of wind conditions that occur at the site. This variability should be considered not only because it influences the wind load characteristics, but also because it is imperative that the proposed methodology performs consistently well regardless of the wind conditions the bridge is exposed to. For the considered data sets, the response is largely dominated by wind effects. Although some contributions from traffic could occur, the traffic density on the bridge is generally low, with a daily average of 1900 crossing vehicles. Vortex shedding effects should be minimal; the box girder is streamlined with guide vanes mounted underneath to mitigate vortex-induced vibrations. The buffeting forces due to turbulence and self-excited forces are expected to be the most significant actions.

For the first recording, Figs. 6 and 7 show the identified forces for modes 1–12 in the time and frequency-domain. The characteristics of the remaining modes (13–18) are similar and are not shown here. For brevity, the identified forces from recording 2–4 are only shown in the frequency-domain (Figs. 8–10). In the frequency domain, the modal forces are similar across the different recordings, although it is expected the actual time-domain evolutions are quite different in terms of local/global extrema, steady level/sudden increase in forces, correlation among modes, etc. All modal forces are largely dominated by the low-frequency components, which is consistent with buffeting loading, although some small peaks are observed at certain frequencies, indicating harmonic components, which manifests mainly for the horizontal-type modes. Self-excitation could lead to such peaks due to natural coupling with the motion of the structure. It should also be noted that in inverse identification, errors in the system model typically lead to spurious peaks in the estimated forces at the natural frequencies since
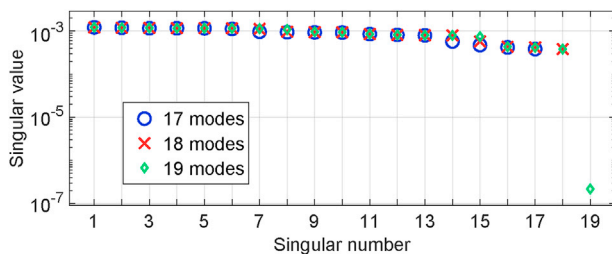
Table 2

Data sets used in the identification of forces.

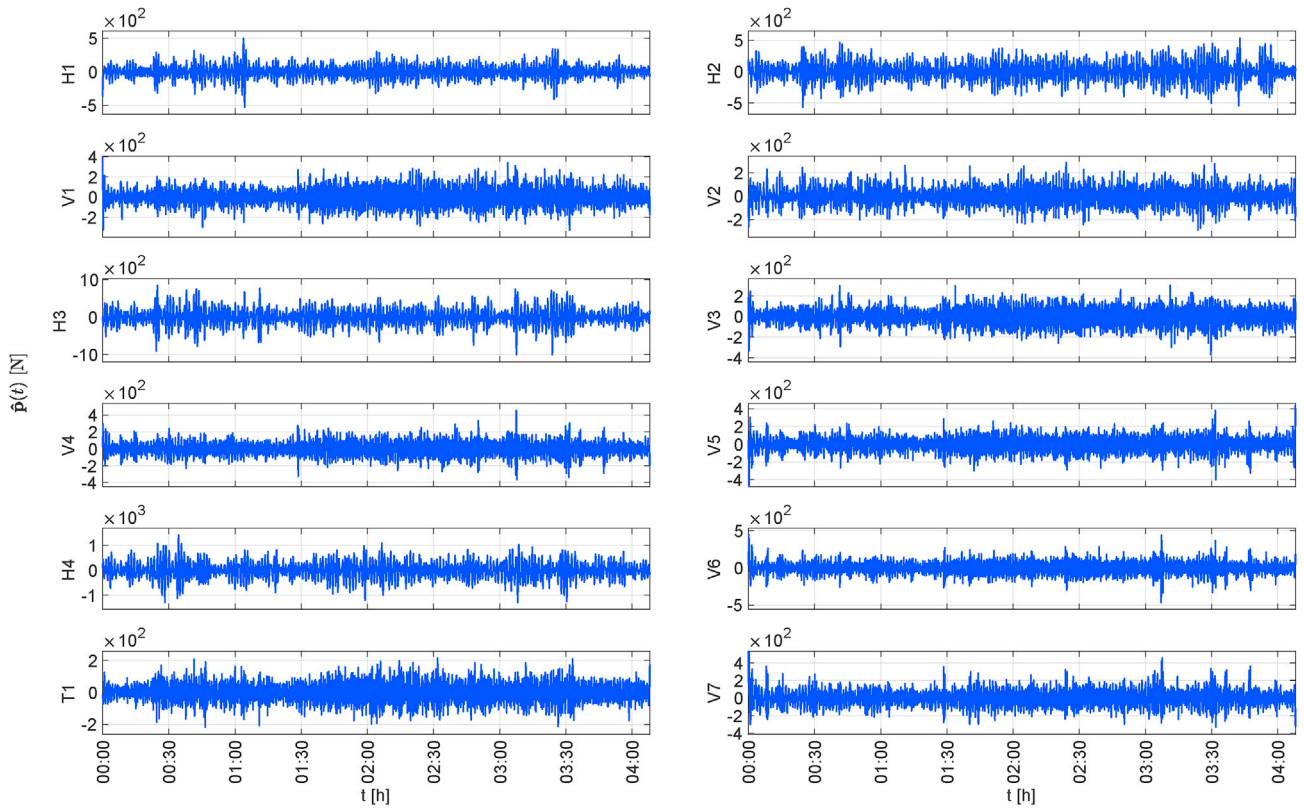| Recording no.	Date and start time	Duration	Mean wind velocity (A6)	Incoming direction
1	2015-03-10 05:59	~ 6 h	~ 10–28 m/s	East
2	2015-05-05 14:53	~ 4 h	~ 10–22 m/s	West
3	2016-01-29 12:30	~ 8 h	~ 15–28 m/s	West
4	2016-12-26 18:09	~ 4 h	~ 10–20 m/s	West

Fig. 6. Identified forces for modes 1–12 in recording 1.

Fig. 7. Fourier transform of the identified forces for modes 1–12 in recording 1. The light blue curve is a smoothed FFT, the star signifies the single natural frequency, the magenta lines signify all natural frequencies, and the green lines signify non-modeled modes. (For interpretation of the references to colour in this figure legend, the reader is referred to the Web version of this article.)
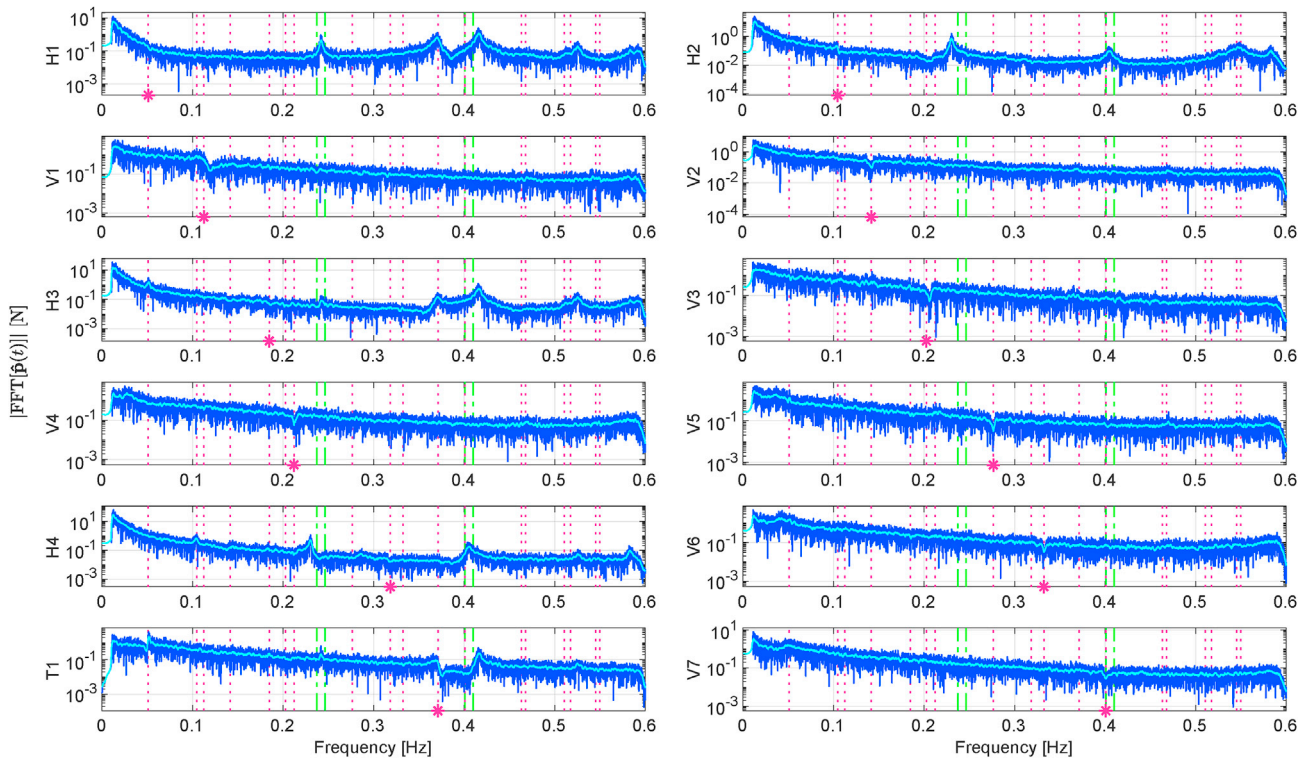
Fig. 8. Fourier transform of the identified forces for modes 1–12 in recording 2. The light blue curve is a smoothed FFT, the star signifies the single natural frequency, the magenta lines signify all natural frequencies, and the green lines signify non-modeled modes. (For interpretation of the references to colour in this figure legend, the reader is referred to the Web version of this article.)
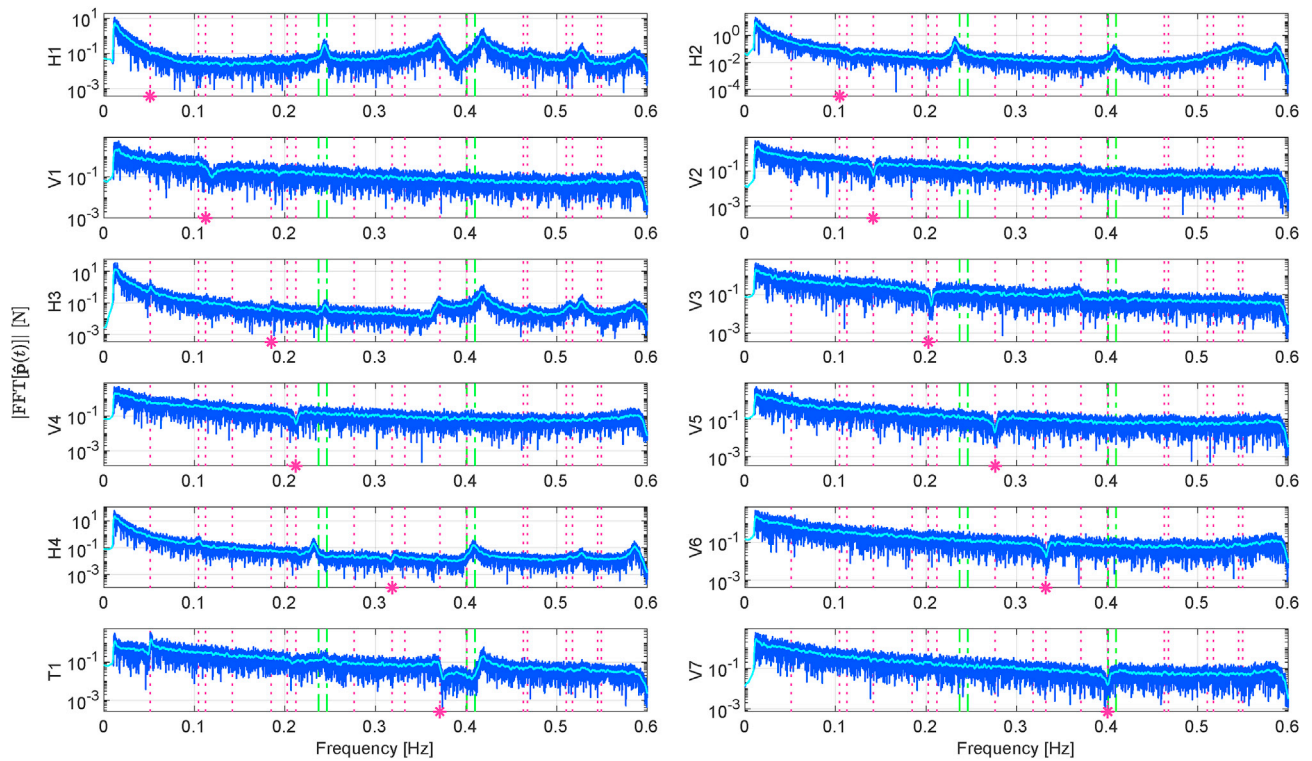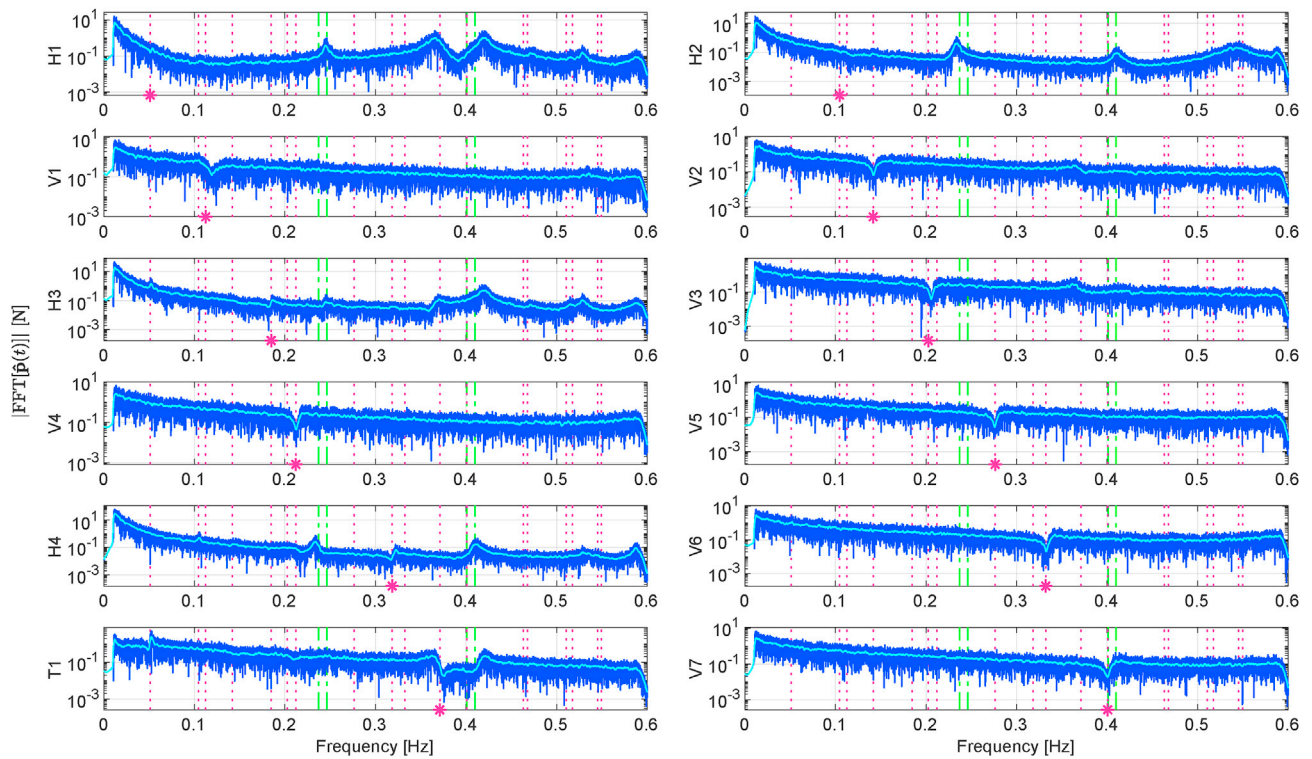

Fig. 9. Fourier transform of identified forces for modes 1–12 in recording 3. The light blue curve is a smoothed FFT, the star signifies the single natural frequency, the magenta lines signify all natural frequencies, and the green lines signify non-modeled modes. (For interpretation of the references to colour in this figure legend, the reader is referred to the Web version of this article.)

Fig. 10. Fourier transform of the identified forces for modes 1–12 in recording 4. The light blue curve is a smoothed FFT, the star signifies the single natural frequency, the magenta lines signify all natural frequencies, and the green lines signify non-modeled modes. (For interpretation of the references to colour in this figure legend, the reader is referred to the Web version of this article.)
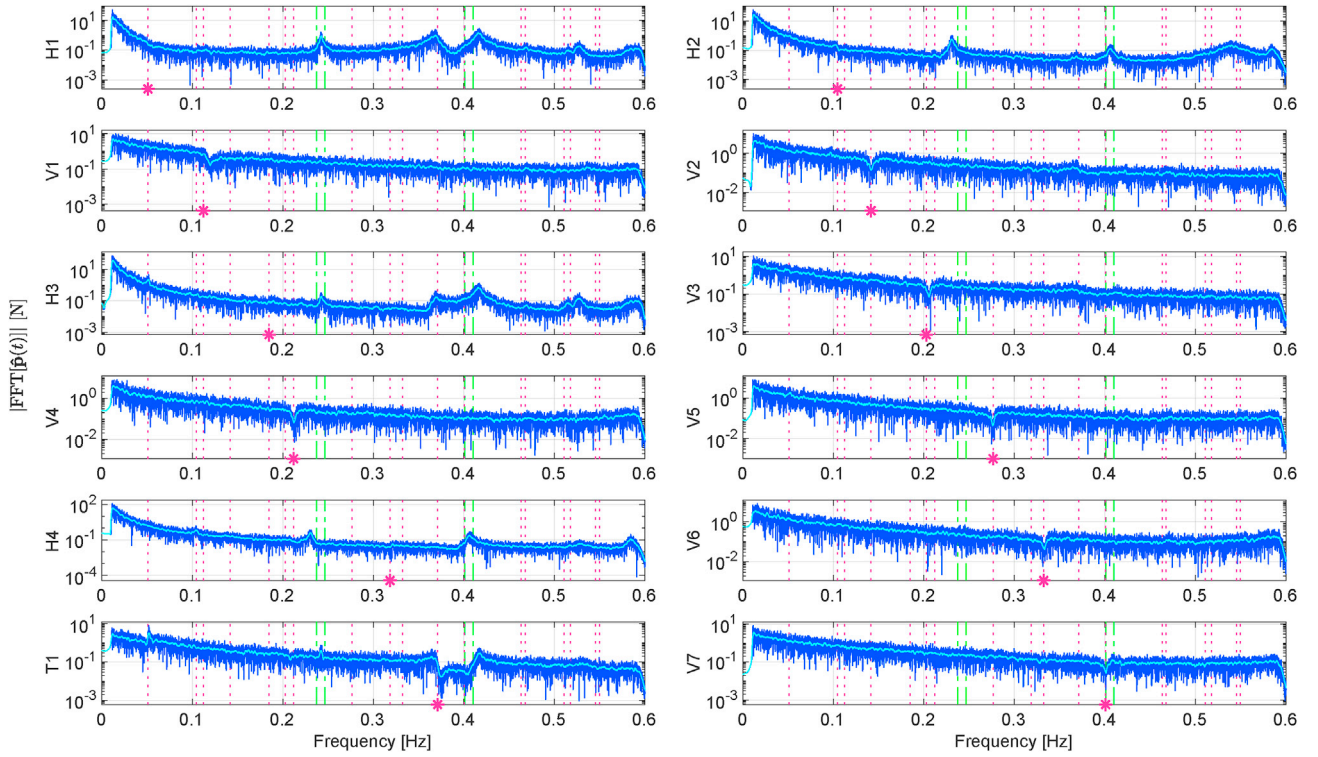
these forces attempt to correct the unexplained behavior of the output data. In this case, four non-modeled modes (i.e., modes not included in the state-space model) from the FE model near 0.24 and 0.4 Hz are indicated in the figures. The deflection of these modes is mainly in the cables with some small movements in the box girder. Neglect of these modes likely causes estimation errors around these frequencies, leading to a blunt peak for the horizontal and torsion modes. Once more, this characteristic points to a limitation in this methodology for cable-supported bridges with a high number of modal contributors and/or the quality of the sensor network.

Consistently, for all recordings, a small dip is observed in the frequency domain at the respective natural frequencies for modes V1–V7 and T1. This dip can be explained by the self-excited effects, which introduce added damping in the vibration modes. Although these dips may appear to be insignificantly small compared to the total force magnitude, they are important since they decrease the forcing around the natural frequency, which significantly reduces the modal response. For most suspension bridges with box girder decks, the vertical modes experience the strongest influence of aerodynamic damping, which is consistent with the observations made here. Furthermore, a sharp-gradient drop is observed for mode T1 at $f = 0.36$ Hz, which is due to the aerodynamic stiffness reduction of the torsional motion. However, this phenomenon becomes mixed with the two non-modeled modes at 0.4 Hz, and the close spacing of the modes hinders a clear interpretation.

Self-excited forces are commonly modeled as proportional to the structural displacements and velocities. These self-excited forces (still in the modal projection space) can actually be obtained from the state estimates by $\widehat{\mathbf{p}}_{se}(t) = [\mathbf{\Phi}^T \mathbf{K}_{ae} \mathbf{\Phi} \quad \mathbf{\Phi}^T \mathbf{C}_{ae} \mathbf{\Phi}] \widehat{\mathbf{x}}(t)$. Depending on the modeling scheme adopted (Chen and Kareem, 2002; Kavrakov and Morgenthal, 2017), the aerodynamic coefficient matrices $\mathbf{K}_{ae}$ and $\mathbf{C}_{ae} \in \mathbb{C}^{n_{DOF}}$ (obtained from wind tunnel tests) are generally dependent on the mean wind velocity (meaning that they will not be time-invariant) in addition to the frequency of the moving structure, so the calculation of $\widehat{\mathbf{p}}_{se}(t)$ becomes a convolution integral due to memory effects. An alternative method

would be to jointly estimate these aerodynamic coefficients with the inputs and states; however, such complex approaches are considered future work and are not pursued here.

3.2. Influence of wind characteristics

Correlating the identified loads with the characteristics of the wind is of great interest. In this context, anemometer data are useful, although the measurements could be seen as a sparse sampling of a large non-sparse wind field. The limited amount of data poses a challenge. The wind forces on the structure depend on the effective wind field along the whole bridge, but only eight sampling locations are available at approximately the elevation of the bridge deck. Although some assumptions or spatial interpolations can be made, the wind velocity field does not have a known low-rank dynamic structure, so the eight measurements alone cannot be used reconstruct the actual properties of the full field. The use of LIDAR technology is an alternative approach that potentially could fill this gap (Cheynet et al., 2017). In the present application, the comparison of the wind measurements and identified forces is therefore of a heuristic type more than an analytical connection.

To make use of the anemometer data, the turbulence and mean wind velocity should be separated while making as few assumptions as necessary. Let $U(t)$ be the along-wind velocity with incoming direction $\theta(t)$, as defined in Fig. 2, and let $W(t)$ be the vertical velocity. We assume that the wind velocity consists of a deterministic time-varying mean value $\overline{U}(t)$, $\overline{W}(t)$ plus a fluctuating component $u(t)$, $w(t)$ that is stochastic:

$$U(t) = \overline{U}(t) + u(t), \quad W(t) = \overline{W}(t) + w(t) \tag{19}$$

We use empirical mode decomposition (EMD) (Xu and Chen, 2004) to characterize the mean wind velocity from the measurement data. First proposed in (Huang et al., 1998), EMD is a data-driven tool that can be used to decompose non-stationary data into a basis set of intrinsic mode functions (IMFs), denoted by $c_j(t)$, through an iterative sifting process;

see, for example, (Xu and Chen, 2004):

$$U(t) = \sum_{j=1}^{N} c_j^{(U)}(t) + r_N^{(U)}(t), \quad W(t) = \sum_{j=1}^{N} c_j^{(W)}(t) + r_N^{(W)}(t) \tag{20}$$

The iterative extraction of the *N* IMFs continues until a stop criterion is met. The final residuals $r_N^{(U)}(t)$ and $r_N^{(W)}(t)$ are treated as the time-varying mean wind velocities $\overline{U}(t)$ and $\overline{W}(t)$, while the sum of the IMFs corresponds to $u(t)$ and $w(t)$. The EMD stop criterion is formulated such that an IMF should not have two consecutive extrema further than 30 min apart; such behavior is viewed as a trend that is so low frequency that it is due to a time-varying mean rather than turbulence. This corresponds to a so-called intermittency check (Huang et al., 1999), where all IMFs consist of frequencies greater than 1/1800 Hz. Since the wind velocity is a fairly broadband process, the number of IMFs is typically $N \approx 6 - 10$.

Figs. 11, 13, 15 and 17 show the wind velocity for anemometer A6 in the middle of the bridge in recordings 1–4; similar results are obtained for the other anemometers. The time-varying trends are captured quite well. Adopting linearized quasi-steady buffeting theory (Scanlan, 1978a; Jain et al., 1996), the buffeting nodal forces ($\mathbf{f}_b(x_i, t) \in \mathbb{R}^3$) on the bridge box girder are approximately proportional to the products $\overline{U}(t)u(t)$ and $\overline{U}(t)w(t)$ at the coordinate $x_i \in [-L/2, L/2]$ along the span $L = 1310$ m:

$$\mathbf{f}_b(x_i, t) = \begin{bmatrix} f_{b,y}(x_i, t) \\ f_{b,z}(x_i, t) \\ f_{b,\theta}(x_i, t) \end{bmatrix} = \frac{\rho B \overline{U}(x_i, t) L_i}{2} \left[2(D/B)\overline{C}_D \, (D/B)C'_D - \overline{C}_L \, 2\overline{C}_L C'_L \right.$$

$$\left. + (D/B)\overline{C}_D \, 2B\overline{C}_M \, BC'_M \right] \begin{bmatrix} u(x_i, t) \\ w(x_i, t) \end{bmatrix} \tag{21}$$

where ρ is the air density, L_i is an influence length, and *B* and *D* are the deck width and height, respectively. The overbar and prime denote the center and gradient in the linearization of the aerodynamic coefficients for drag, lift and moment around the mean angle of attack. The effects of the admittance functions are not considered here. Equivalently, the total modal buffeting forces become:

$$\mathbf{p}_b(t) = \boldsymbol{\Phi}^T \mathbf{S}_b [\mathbf{f}_b(x_1, t)^T \cdots \mathbf{f}_b(x_i, t)^T \cdots \mathbf{f}_b(x_M, t)^T]^T \tag{22}$$

with $\mathbf{S}_b \in \mathbb{R}^{n_{\text{DOF}} \times 3M}$ selecting the set of *M* loaded nodal DOFs. As

mentioned previously, the wind is measured at only eight locations along the span ($x = \{460, 280, 240, 200, 180, -10, -180, 420\}$ m), so the quantities in Eq. (22) are not fully known. Despite this limitation, $\overline{U}(t)u(t)$ and $\overline{U}(t)w(t)$ represent the approximate intensity of the buffeting forces. Here, the short-term "averaged intensity" is quantified by the help of a moving window root mean square (MW-RMS) metric, defined for an arbitrary function $a(t)$ as the integral:

$$\text{MW} - \text{RMS}[a(t)] = \sqrt{\frac{1}{T_w} \int_{t-T_w/2}^{t+T_w/2} a(\tau)^2 \, d\tau} \tag{23}$$

where the centralized window is set to $T_w = 60$ s. For a fair comparison with the forces, the time series for $u(t)$ and $w(t)$ are also high-pass filtered at 0.01 Hz in this calculation.

Figs. 12, 14, 16 and 18 show the MW-RMS for the wind turbulence products $\overline{U}(t)u(t)$ and $\overline{U}(t)w(t)$ at anemometers A1-A8, together with the identified modal forces ($\hat{\mathbf{p}}(t)$). For the latter, the MW-RMS is normalized to unity for the individual modal component because magnitude differences prohibit a clear comparison. Note that the turbulence illustrations in these figures do not tell the full story since their net effect on the bridge will depend on the spatial correlations in relation to the shape of the individual mode. Still, some interesting concurrent trends can be observed.

In recording 1 (Fig. 12), the wind comes from the eastern sector $\theta \in [45°, 90°]$. The onset of the skew-most wind around $t \approx 1:30$ h also coincides with the large turbulence, in particular for A1-A5, which can likely be explained by the path of the wind across the tall mountains on the south side of the fjord (cf. Fig. 2). This skew wind and its load effects are interesting since wind tunnels tests of section models with proportions similar to the Hardanger bridge have indicated a significant dependency on the skew angle and the angle of attack (Zhu et al., 2002). However, from these load estimates, it is difficult to distinguish the effects related to a single environmental variable since the presence or evolution of multiple variables cannot be controlled separately. In this case, small load effects purely from the skewness are likely to be masked by the simultaneously occurring strong turbulence, which that has a larger influence on the buffeting forces. The clear inhomogeneities in the wind field could also play a role. Earlier studies have indicated that inhomogeneities occur due to the local topology, and in this regard, the eastern and western winds tend to have different patterns (Lystad et al., 2018).
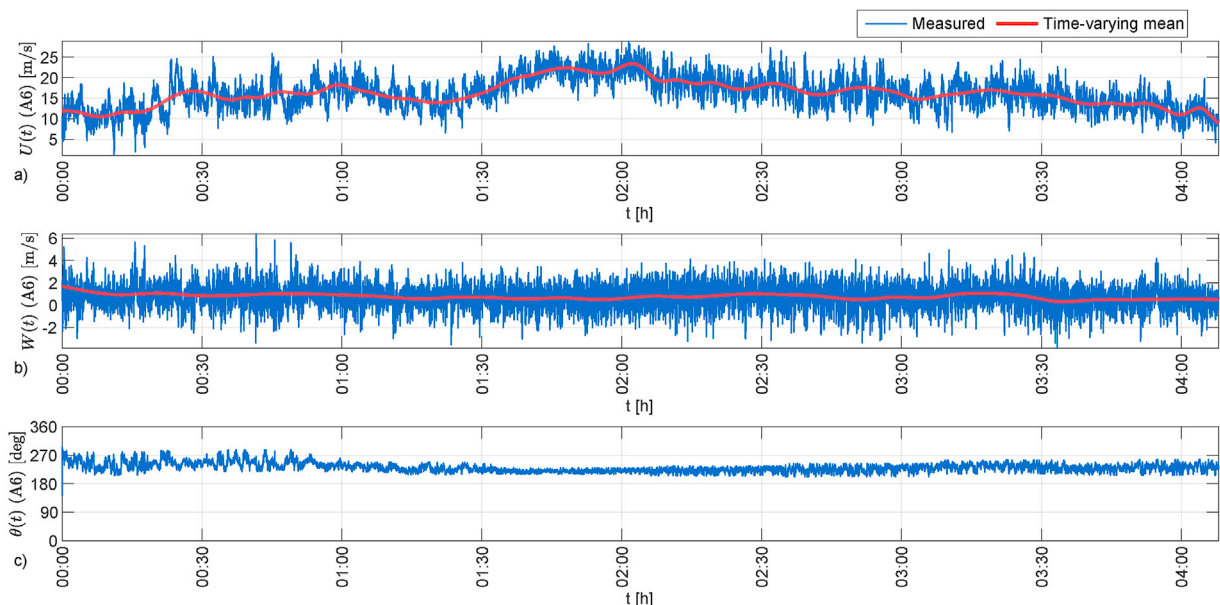

Fig. 11. Measurements from anemometer A6 in recording 1: a) along-wind velocity; b) vertical wind velocity; c) direction.
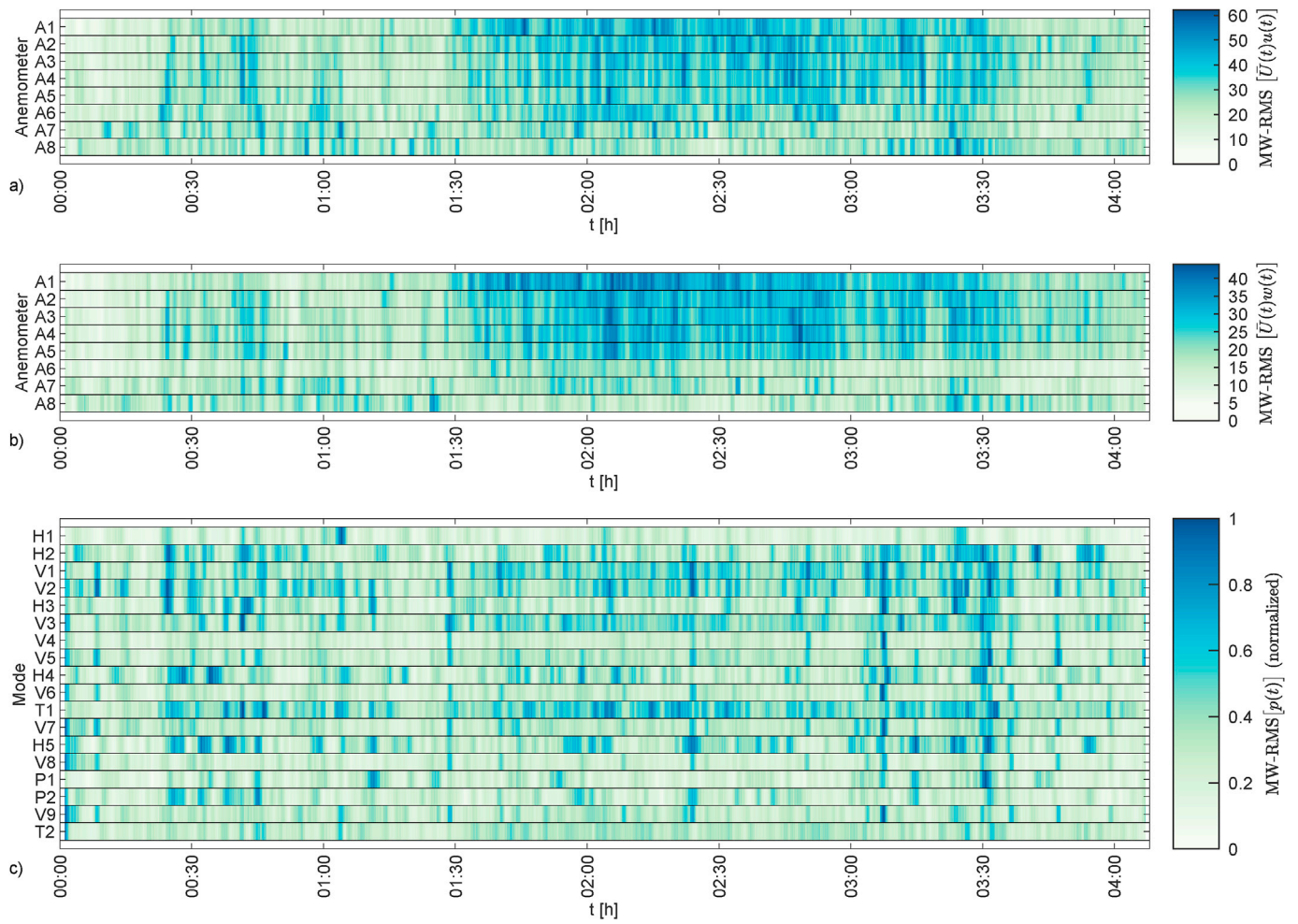
Fig. 12. Comparison of the time evolution in recording 1: a) along-wind turbulence; b) vertical turbulence; c) identified modal forces.

Fig. 13. Measurements from anemometer A6 in recording 2: a) along-wind velocity; b) vertical wind velocity; c) direction.

Fig. 14. Comparison of the time evolution in recording 2: a) along-wind turbulence; b) vertical turbulence; c) identified modal forces.
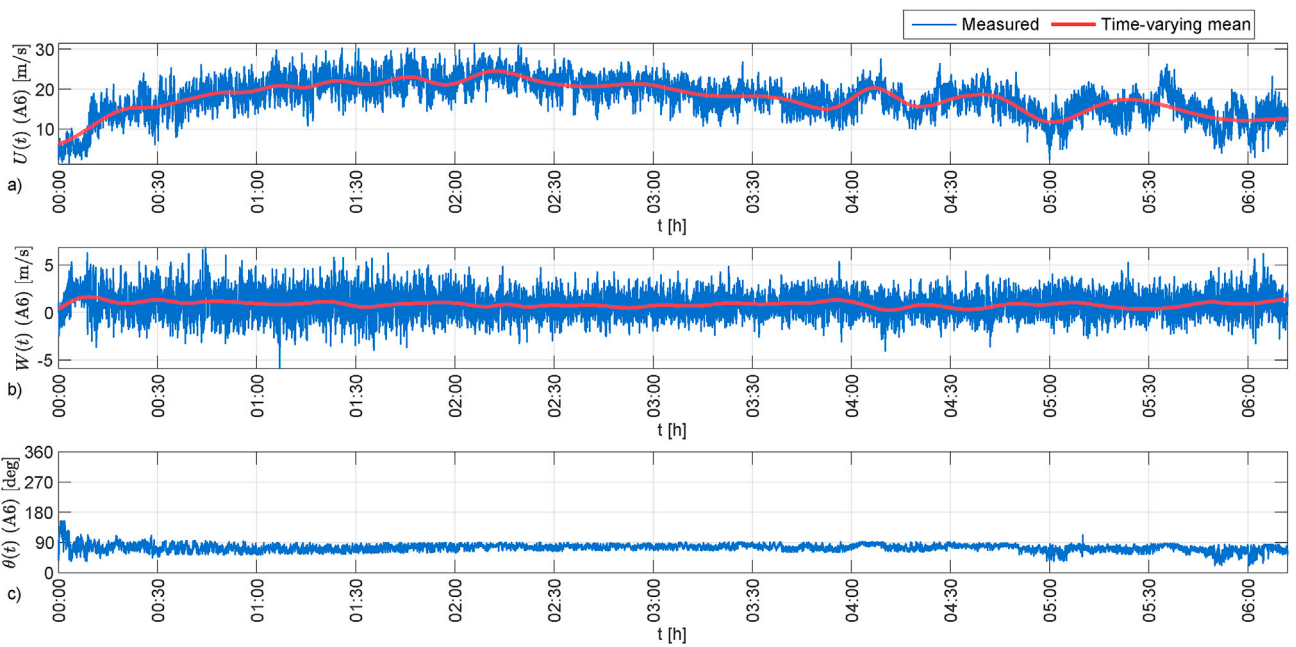

Fig. 15. Measurements from anemometer A6 in recording 3: a) along-wind velocity; b) vertical wind velocity; c) direction.

Fig. 16. Comparison of the time evolution in recording 3: a) along-wind turbulence; b) vertical turbulence; c) identified modal forces.

Fig. 17. Measurements from anemometer A6 in recording 4: a) along-wind velocity; b) vertical wind velocity; c) direction.
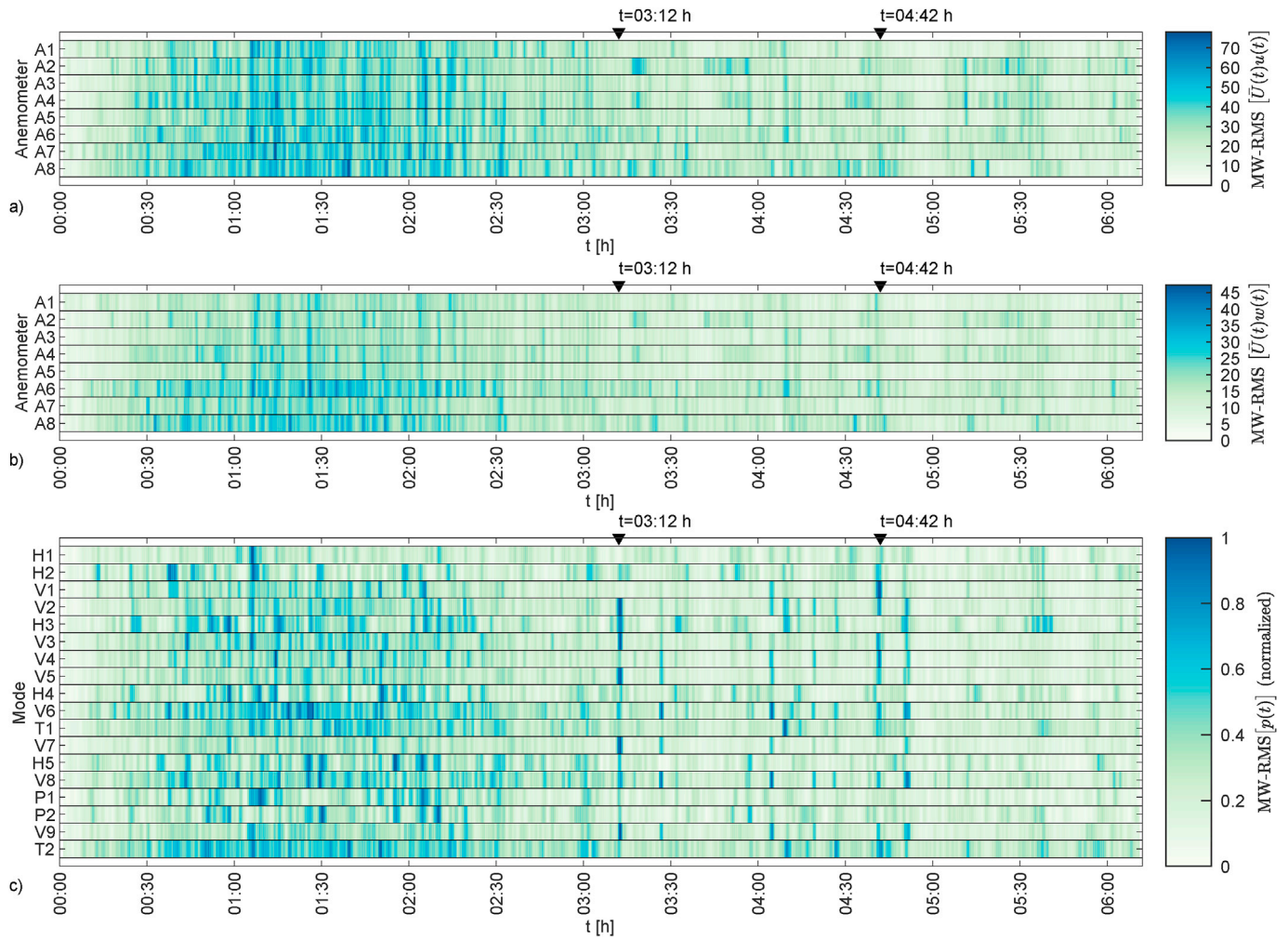
Fig. 18. Comparison of the time evolution in recording 4: a) along-wind turbulence; b) vertical turbulence; c) identified modal forces.
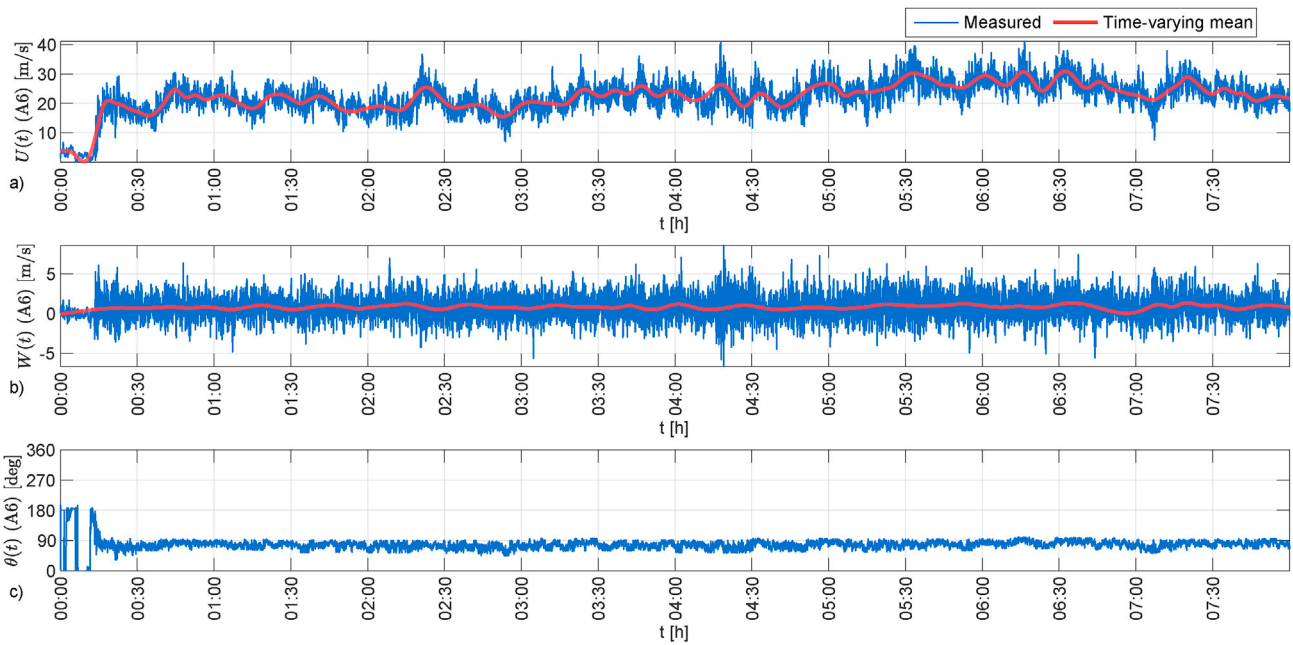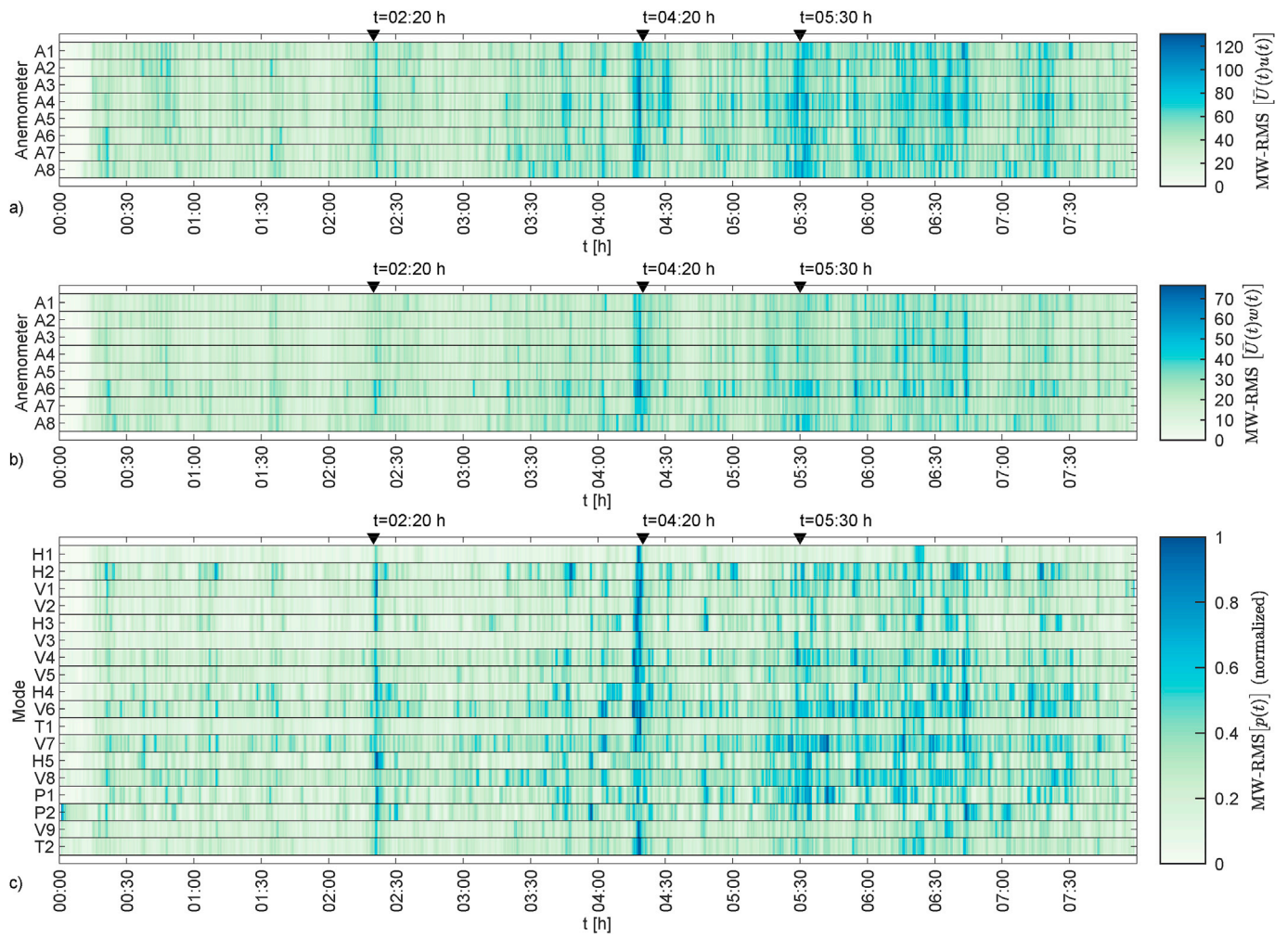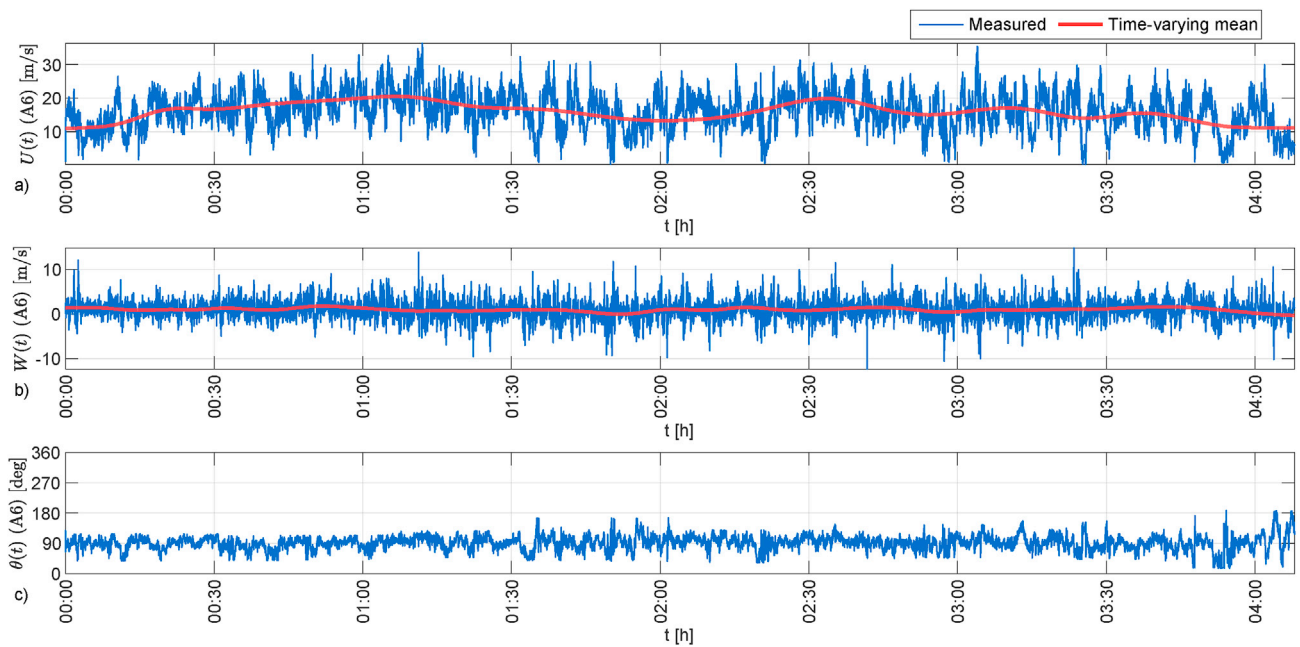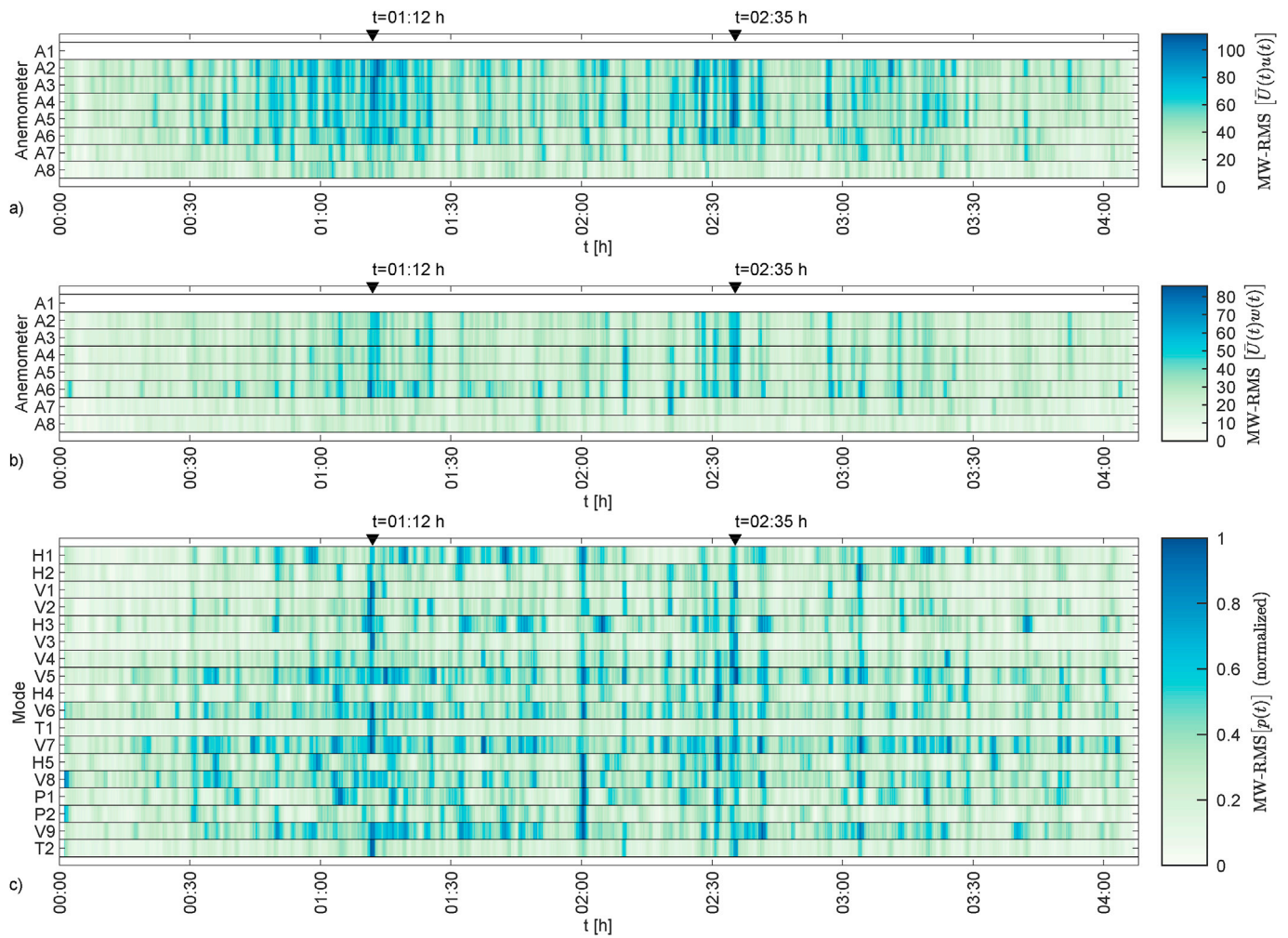
In recording 2 (Fig. 14), a more homogeneous wind field is observed, although the north side (A6-A8) appears to have slightly more turbulence. Moreover, the influence of the turbulence for $t \in [0 : 30, 2 : 30]$ h clearly manifests in the loads. Later, some large loads occur seemingly without any large turbulence at the time, for instance, at $t = \{3 : 12, 4 : 42\}$ h. The exact reason for these loads is not known, but a closer examination of the anemometer time series for A1 and A2 indicates some strong local gusts with duration of less than 5 s, which are not easily detected with an averaging window of 60 s.

In recording 3 (Fig. 16), the load is almost zero for the first 15 min, when the wind starts to increase. The influence of strong and along-span correlated turbulence can be observed at several time instants. At $t = 2 : 20$ h, the effect of an along-wind gust is clearly visible in the forces, and again, more pronounced at $t = 4 : 20$ h. Aided by strong vertical turbulence, almost all the modal forces reach the maximum magnitude at the same time. For reference, the maximum horizontal deflection in the midspan reaches almost 8 m, and the estimated stress in the box girder at this time reaches a maximum well over 100 MPa, which testifies to the harsh impact felt by the structure. In the later period ($t > 4 : 30$ h), some strong but not fully correlated gusts still occur, for instance, around $t \approx 5 : 30$ h, which still leads to some large forces but not for all modes.

In the last recording (Fig. 18), quite inhomogeneous wind conditions are observed. Although the data from A1 are missing, the wind at A2-A6 (south side) is considerably more turbulent. Correlations in the wind and forces are evident at the two indicated times $t = \{1 : 12, 2 : 35\}$ h. However, the strong forces occurring at $t = 2 : 00$ h cannot be explained directly by the turbulence in this figure.

3.3. Comparison with other algorithms and design wind load spectrum

The results in the previous sections show some potential issues in the identification of the forces; therefore, it is interesting to compare other approaches to check whether they are better suited. In this section, two additional inverse methods are considered. The first is a dual Kalman filter (Azam et al., 2015), which is distinct due to its stable estimation of the acceleration output only. In this algorithm, the force has a statistical evolution model of the form $\mathbf{p}_{k+1} = \mathbf{p}_k + \eta_k$, where the fictitious process η_k is a zero-mean white noise vector with covariance $\mathbb{E}[\eta_k \eta_l^{\mathrm{T}}] = \mathbf{Q}_p \delta_{kl}$. This covariance is deemed a regularization parameter that controls the force solution norm. In this case, a tuned value of $\mathbf{Q}_p = 10^{-1}\mathbf{I}$ yields the best fit to the output data (minimum innovation norm).

Second, we apply a sequential deconvolution reconstruction (SDR) of the inputs (Bernal and Ussia, 2015). While the JIS and DKF are based on one-step recursive estimation, this method utilizes a sliding window for time-domain deconvolution and is therefore computationally efficient. The size of the window and the rate of advance are, respectively, set to $40\Delta t$ and $20\Delta t$ according to their definitions in (Bernal and Ussia, 2015). Note that the SDR uses a deterministic system model, thus neglecting the stochastic noise ($\mathbf{Q}, \mathbf{R}, \mathbf{S} = 0$).

The results in Fig. 19 from the time period $t \in [2 : 30, 3 : 00]$ in recording 2 display a representative image of the performance. Interestingly, the deterministic method SDR provides estimates that are consistent with the JIS, which formally has a stronger capability due to the consideration of stochastic noise. This outcome is believed to be the result of the use of modal forces rather than localized forces. Since a
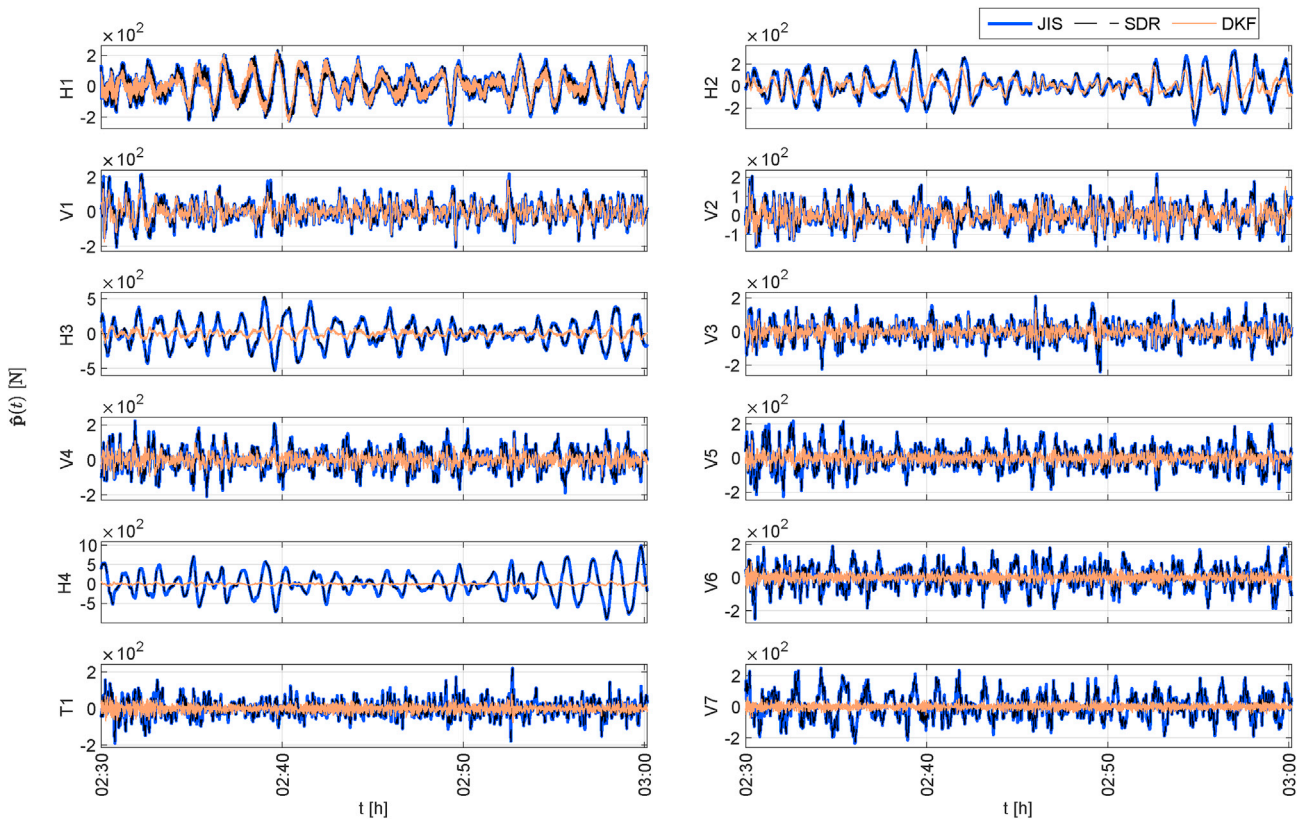
Fig. 19. Identified forces for modes 1–12 for a 30 min period of recording 2.
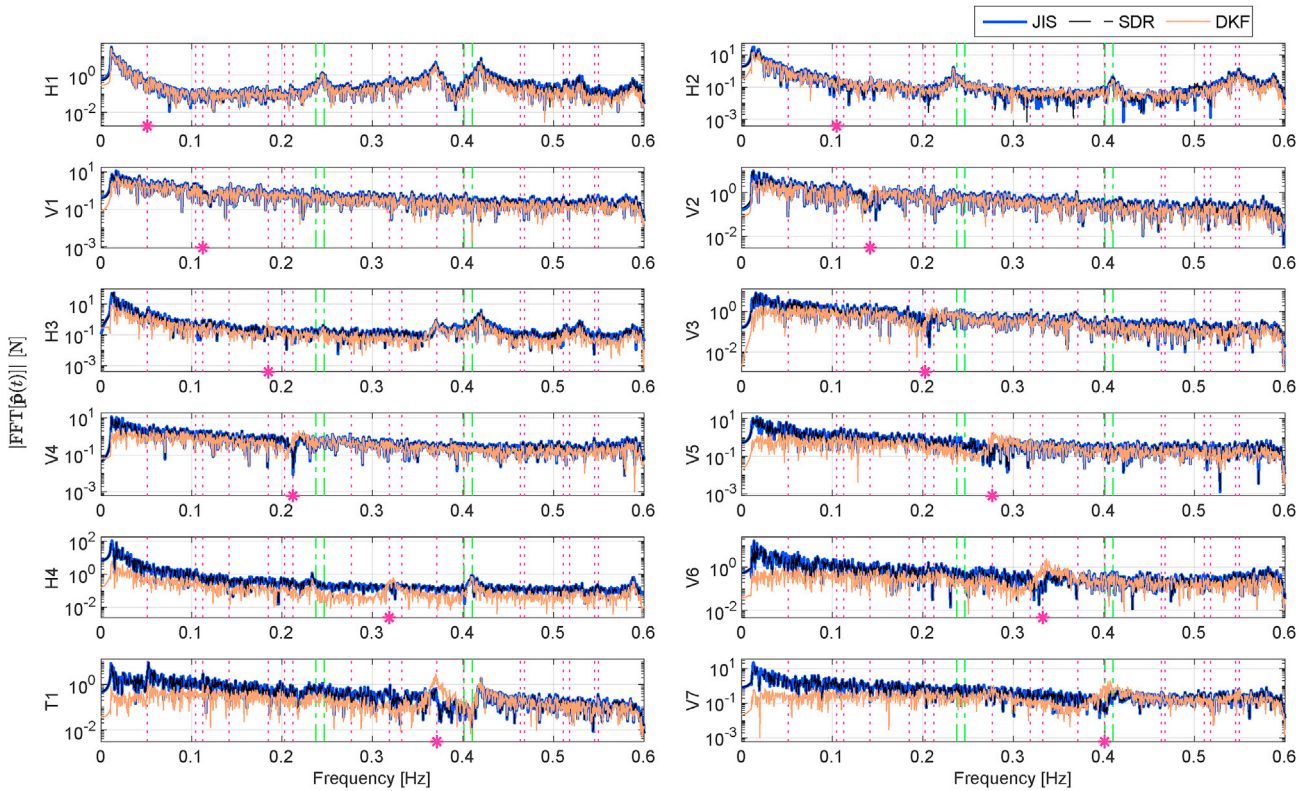

Fig. 20. Identified forces for modes 1–12 for a 30 min period of recording 2. The star signifies the single natural frequency, the magenta lines signify all natural frequencies, and the green lines signify non-modeled modes. (For interpretation of the references to colour in this figure legend, the reader is referred to the Web version of this article.)

modal force theoretically is a summation of the forces in all positions, it can more easily smooth model errors, whereas a localized force has influence only in its vicinity. The DKF generally gives lower values, an effect that increases for higher modes for reasons that are not well understood. From Fig. 20, it can be concluded that the difference is largely due to the low-frequency discrepancy. Another observation is that the DKF does not have a dip at the natural frequency (added damping from self-excitation) but instead has an increased magnitude, which is believe to be unrealistic. Scaling the covariance $\mathbf{Q}_p$ changes the overall force magnitude but not the frequency-domain characteristics. A robust method for choosing this covariance in scenarios with many forces (possibly having different evolutions) is not available at the moment.

Next, a brief comparison is made with the loads predicted from the design wind field model based on a Kaimal spectrum (see (Fenerci and Øiseth, 2017) for details). Herein, the static coefficients are set to the following values obtained from wind tunnel tests (Siedziako et al., 2017): $\overline{C}_D = 1.05$, $C'_D = 0$, $\overline{C}_L = -0.363$, $C'_L = 2.22$, $\overline{C}_M = -0.017$, $C'_M = 0.786$. The bridge deck has the proportions $B = 18.3$ m and $D = 3.25$ m. In this context, this classic wind load modeling approach is called the "forward analysis", since its basis is the wind velocity field yielding the loads on the bridge. In contrast, the inverse estimation of the wind loads is driven by the measured acceleration data. These two approaches are fundamentally different, but both independently result in the wind load quantification. In the forward analysis the wind loads can be described only stochastically, so spectral densities in the frequency domain are employed. The buffeting plus self-excited forces are defined as:

$$\mathbf{f}(\omega) = \mathbf{f}_b(\omega) + \mathbf{C}_{ae}\dot{\mathbf{u}}(\omega) + \mathbf{K}_{ae}\mathbf{u}(\omega) \tag{24}$$

For simplicity, $\mathbf{C}_{ae}$ and $\mathbf{K}_{ae}$ are taken from quasi-steady theory in the following (see e.g. (Kavrakov and Morgenthal, 2017)). The (total) generalized forces, $\mathbf{p}(\omega) = \mathbf{\Phi}^T\mathbf{f}(\omega)$, can then be written as:

$$\mathbf{p}(\omega) = \mathbf{p}_b(\omega) + \tilde{\mathbf{C}}_{ae}\dot{\mathbf{z}}(\omega) + \tilde{\mathbf{K}}_{ae}\mathbf{z}(\omega) \tag{25}$$

where $\tilde{\mathbf{C}}_{ae} = \mathbf{\Phi}^T\mathbf{C}_{ae}\mathbf{\Phi}$ and $\tilde{\mathbf{K}}_{ae} = \mathbf{\Phi}^T\mathbf{K}_{ae}\mathbf{\Phi}$. Utilizing $\mathbf{z}(\omega) = \tilde{\mathbf{H}}(\omega)\mathbf{p}_b(\omega)$, Eq. (25) can be written as:

$$\mathbf{p}(\omega) = (\mathbf{I} + (i\omega\tilde{\mathbf{C}}_{ae} + \tilde{\mathbf{K}}_{ae})\tilde{\mathbf{H}}(\omega))\mathbf{p}_b(\omega) \tag{26}$$

where the generalized transfer function is $\tilde{\mathbf{H}}(\omega) = [-\omega^2\mathbf{I} + i\omega(2\mathbf{\Xi}\mathbf{\Omega} - \tilde{\mathbf{C}}_{ae}) + (\mathbf{\Omega}^2 - \tilde{\mathbf{K}}_{ae})]^{-1}$. Only wind loads on the girder are taken into account due to the lack of data on the wind characteristics at the elevation of the main cables. Assuming the spectrum $\mathbf{S}_{f_bf_b}(\omega) \in \mathbb{C}^{n_{DOF}\times n_{DOF}}$ of the buffeting forces (Eq. (21)) is available, the generalized force spectrum $\mathbf{S}_{pp}(\omega) \in \mathbb{C}^{n_m\times n_m}$ can finally be calculated as:

$$\mathbf{S}_{pp}(\omega) = (\mathbf{I} + (i\omega\tilde{\mathbf{C}}_{ae} + \tilde{\mathbf{K}}_{ae})\tilde{\mathbf{H}}(\omega))^H\mathbf{\Phi}^T\mathbf{S}_{f_bf_b}(\omega)\mathbf{\Phi}(\mathbf{I} + (i\omega\tilde{\mathbf{C}}_{ae} + \tilde{\mathbf{K}}_{ae})\tilde{\mathbf{H}}(\omega)) \tag{27}$$

Fig. 21 compares the force spectra from the forward prediction and the inverse estimate using data from the time period $t \in [2:30, 3:00]$ in recording 2, in which the wind is normal to the bridge. Averaging over this 30 min period, the mean wind velocity is $\overline{U} = 21.2$ m/s, and the turbulence intensities are $I_u = \sigma_u/\overline{U} = 0.096$ and $I_w = \sigma_w/\overline{U} = 0.035$. Although the results inevitably vary for different events, the time period shown has reasonably ideal (homogeneous and stationary) wind conditions and should yield a fair comparison. However, the design wind field model has many uncertain features that do not always match the observed wind characteristics at the site (Fenerci et al., 2017); thus, the presented frequency-domain inquiry is a simple test to get an idea of the similarity and cannot be considered a strict tool for validation.

Overall, the degree of (dis)agreement in Fig. 21 is as expected for the inverse force identification of full-scale bridges in complex and uncertain conditions, which has not been extensively explored. For the JIS modal force estimate, the magnitude appears to match best at the individual natural frequency. In the frequency range far below the natural frequency, the DKF estimate agrees better, and the JIS yields a higher magnitude. This result could either be due to an estimation error or
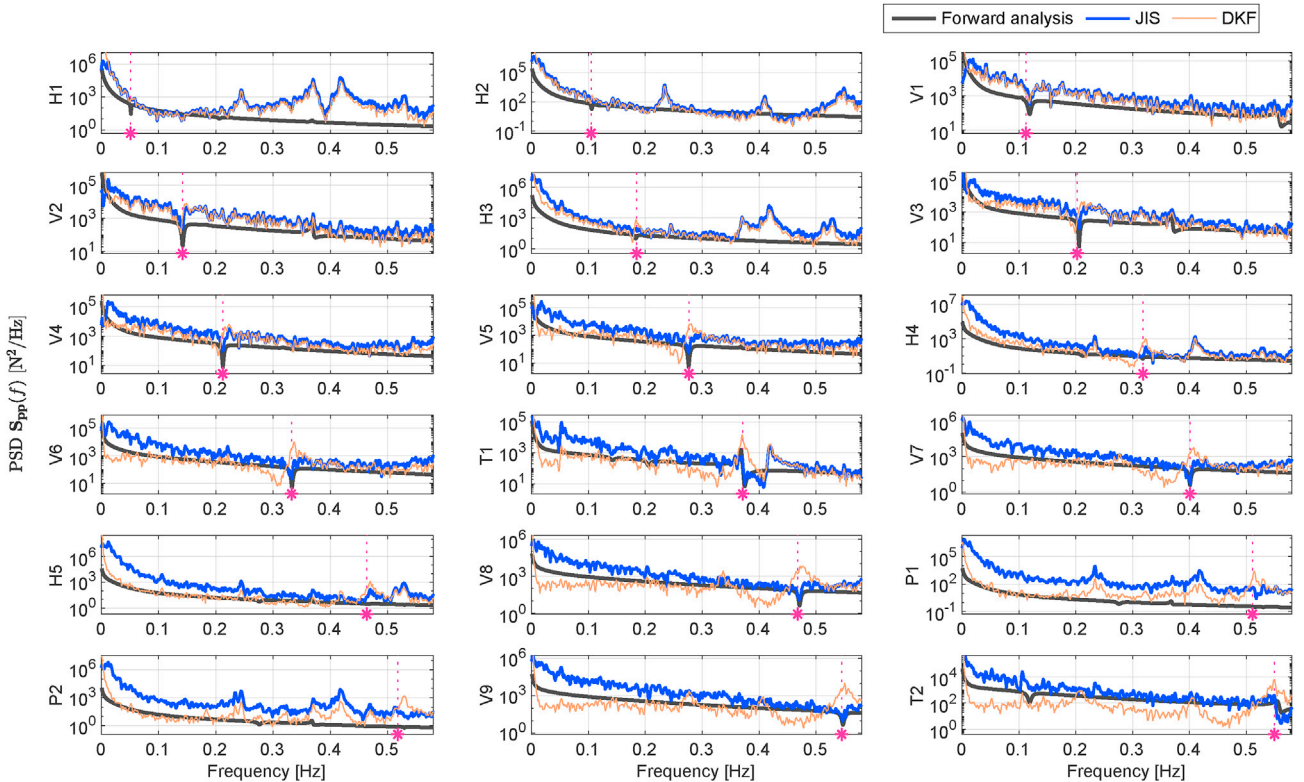

Fig. 21. Comparison between the spectral density of the inverse load estimates (averaged by Welch's method) and the forward model prediction of the wind loads. The star and the magenta line signify the natural frequency.

actual behavior. As discussed in Section 2.3, acceleration outputs are not always well suited for estimating very-low-frequency forces due to their ω^2-proportionality, which becomes small for close-to-static motion. The insensitivity could lead to a (frequency-banded) low signal-to-noise ratio, which is known to be particularly disruptive for inverse problems. Therefore, displacements or strains are more useful for this purpose; however, latent sensor noise is believed to play only a small role here. The behavior can potentially be explained by some slow fluctuations in the mean wind velocity. Such fluctuations are typically not captured in the forward analysis that considers stationary conditions (constant mean wind velocity).

3.4. Evaluation of methodology and usefulness of obtained load information

No real direct validation of the estimated forces is available at this scale, so the uncertainties are difficult to quantify. Promising progress has been made in understanding the application to suspension bridges, but the case study also shows some robustness issues with the estimation algorithms, as well as the need for extensive sensor networks to achieve a high level of confidence in the results. Regardless, application robustness is, for this bridge, far better than that for a similar study on floating bridges (Petersen et al., 2019), where the model uncertainties are far greater.

Although the data of the load and response behavior can be useful, an obvious dilemma is that measurements cannot be made before the structure is built, at which point it has already been designed based on wind tunnel testing and wind field analysis, and major alterations cannot be conveniently made. Thus, the methodology is more suited to research and validation studies on existing bridges or simply to monitoring response behavior throughout the lifetime. The body of knowledge gained from the lessons from existing bridges is also a valuable stepping stone that could facilitate the design of future bridges.

The methodology is also promising for studies of the loads in more unusual events that do not fit the ordinary set of wind modeling assumptions. The load mechanisms for bridges in highly non-stationary downbursts in thunderstorms, for example, are not well documented (Chen and Letchford, 2005; Solari et al., 2015). In theory, the input and state estimation could also be extended to parameter estimation to indicate damage (stiffness reduction), but this task remains difficult because modal sensitivity to local damage is generally very small for long-span bridges.

4. Conclusions

This article has presented the inverse identification of dynamic wind loads from measured response data, focusing on the Hardanger bridge, a long-span suspension bridge instrumented with accelerometers. The methodology does not impose any prior assumptions on the wind loading, as loads are estimated directly from acceleration data using an algorithm for joint input and state estimation.

Overall, the frequency-domain characteristics of the estimated loads appear to be realistic, except for the effect of some known errors in the reduced-order modal model. The magnitudes of the estimated loads are higher than predicted directly from design wind field models. Buffeting and self-excited forces are both distinctly present, but these factors are estimated jointly and cannot currently be separated. When compared with the anemometer data, clear simultaneous trends between the time series of the estimated modal forces and wind turbulence are observed. The results suggest that the methodology, if further developed and tested, could be useful in the characterization of wind loads on bridges with uncertain wind conditions.

Some practical and theoretical limitations lead to issues that should be addressed. The number of modal forces that can be reconstructed is limited by the output data. Since long-span bridges have many modes

with significant wind-induced excitation, a large and well-designed sensor network is required to reconstruct the total dynamical behavior. The estimation based on acceleration data also constitutes a limitation in studies of wind loads, as close-to-static forces are not always well estimated. This source of uncertainty could be eliminated if strain measurements were added.

References

Amiri, A.K., Bucher, C., 2017. A procedure for in situ wind load reconstruction from structural response only based on field testing data. J. Wind Eng. Ind. Aerodyn. 167, 75–86.

Aucejo, M., De Smet, O., Deü, J.F., 2018. On a space-time regularization for force reconstruction problems. Mech. Syst. Signal Process. 118, 549–567.

Aucejo, M., De Smet, O., Deü, J., 2018. Practical issues on the applicability of Kalman filtering for reconstructing mechanical sources in structural dynamics. J. Sound Vib. 442, 45–70.

Azam, S.E., Chatzi, E., Papadimitriou, C., 2015. A dual Kalman filter approach for state estimation via output-only acceleration measurements. Mech. Syst. Signal Process. 60, 866–886.

Bernal, D., Ussia, A., 2015. Sequential deconvolution input reconstruction. Mech. Syst. Signal Process. 50, 41–55.

Bietry, J., Delaunay, D., Conti, E., 1995. Comparison of full-scale measurement and computation of wind effects on a cable-stayed bridge. J. Wind Eng. Ind. Aerodyn. 57, 225–235.

Caracoglia, L., 2008. Influence of uncertainty in selected aerodynamic and structural parameters on the buffeting response of long-span bridges. J. Wind Eng. Ind. Aerodyn. 96, 327–344.

Chang, X., Yan, Y., Wu, Y., 2019. Study on solving the ill-posed problem of force load reconstruction. J. Sound Vib. 440, 186–201.

Chen, X., Kareem, A., 2002. Advances in modeling of aerodynamic forces on bridge decks. J. Eng. Mech. 128, 1193–1205.

Chen, L., Letchford, C., 2005. Proper orthogonal decomposition of two vertical profiles of full-scale nonstationary downburst wind speeds [lzcl]. J. Wind Eng. Ind. Aerodyn. 93, 187–216.

Cheynet, E., Jakobsen, J.B., Snæbjörnsson, J., 2016. Buffeting response of a suspension bridge in complex terrain. Eng. Struct. 128, 474–487.

Cheynet, E., Jakobsen, J.B., Snæbjörnsson, J., Reuder, J., Kumer, V., Svardal, B., 2017. Assessing the potential of a commercial pulsed lidar for wind characterisation at a bridge site. J. Wind Eng. Ind. Aerodyn. 161, 17–26.

Cigada, A., Falco, M., Zasso, A., 2001. Development of new systems to measure the aerodynamic forces on section models in wind tunnel testing. J. Wind Eng. Ind. Aerodyn. 89, 725–746.

Diana, G., Resta, F., Zasso, A., Belloli, M., Rocchi, D., 2004. Forced motion and free motion aeroelastic tests on a new concept dynamometric section model of the Messina suspension bridge. J. Wind Eng. Ind. Aerodyn. 92, 441–462.

Fenerci, A., Øiseth, O., 2017. Measured buffeting response of a long-span suspension bridge compared with numerical predictions based on design wind spectra. J. Struct. Eng. 143, 04017131.

Fenerci, A., Øiseth, O., Rønnquist, A., 2017. Long-term monitoring of wind field characteristics and dynamic response of a long-span suspension bridge in complex terrain. Eng. Struct. 147, 269–284.

Huang, N.E., Shen, Z., Long, S.R., Wu, M.C., Shih, H.H., Zheng, Q., Yen, N.-C., Tung, C.C., Liu, H.H., 1998. The empirical mode decomposition and the Hilbert spectrum for nonlinear and non-stationary time series analysis. Proc. R. Soc. Lond.: Math. Phys. Eng. Sci. 454, 903–995.

Huang, N.E., Shen, Z., Long, S.R., 1999. A new view of nonlinear water waves: the Hilbert spectrum. Annu. Rev. Fluid Mech. 31, 417–457.

Hwang, J., Kareem, A., Kim, H., 2011. Wind load identification using wind tunnel test data by inverse analysis. J. Wind Eng. Ind. Aerodyn. 99, 18–26.

Jacquelin, E., Bennani, A., Hamelin, P., 2003. Force reconstruction: analysis and regularization of a deconvolution problem. J. Sound Vib. 265, 81–107.

Jain, A., Jones, N.P., Scanlan, R.H., 1996. Coupled flutter and buffeting analysis of long-span bridges. J. Struct. Eng. 122, 716–725.

Jakobsen, J., Tanaka, H., 2003. Modelling uncertainties in prediction of aeroelastic bridge behaviour. J. Wind Eng. Ind. Aerodyn. 91, 1485–1498.

Kang, N., Kim, H., Choi, S., Jo, Seongwoo, Hwang, J.-S., Yu, E., 2012. Performance evaluation of TMD under typhoon using system identification and inverse wind load estimation. Comput. Aided Civ. Infrastruct. Eng. 27, 455–473.

Kavrakov, I., Morgenthal, G., 2017. A comparative assessment of aerodynamic models for buffeting and flutter of long-span bridges. Engineering 3, 823–838.

Ko, J., Ni, Y., 2005. Technology developments in structural health monitoring of large-scale bridges. Eng. Struct. 27, 1715–1725.

Lai, T., Yi, T.-H., Li, H.-N., Fu, X., 2017. An explicit fourth-order Runge–Kutta method for dynamic force identification. Int. J. Struct. Stab. Dyn. 1750120.

Larsen, A., Larose, G.L., 2015. Dynamic wind effects on suspension and cable-stayed bridges. J. Sound Vib. 334, 2–28.

Li, K., Liu, J., Han, X., Sun, X., Jiang, C., 2015. A novel approach for distributed dynamic load reconstruction by space–time domain decoupling. J. Sound Vib. 348, 137–148.

Liu, Y., Shepard Jr., W.S., 2005. Dynamic force identification based on enhanced least squares and total least-squares schemes in the frequency domain. J. Sound Vib. 282, 37–60.

Lourens, E., 2012. Force Identification in Structural Dynamics. Ph.D. thesis. Katholieke Universiteit Leuven - Faculty of Engineering, Leuven (Belgium).

Lourens, E., Reynders, E., De Roeck, G., Degrande, G., Lombaert, G., 2012. An augmented Kalman filter for force identification in structural dynamics. Mech. Syst. Signal Process. 27, 446–460.

Lourens, E., Papadimitriou, C., Gilljns, S., Reynders, E., De Roeck, G., Lombaert, G., 2012. Joint input-response estimation for structural systems based on reduced-order models and vibration data from a limited number of sensors. Mech. Syst. Signal Process. 29, 310–327.

Lystad, T.M., Fenerci, A., Øiseth, O., 2018. Evaluation of mast measurements and wind tunnel terrain models to describe spatially variable wind field characteristics for long-span bridge design. J. Wind Eng. Ind. Aerodyn. 179, 558–573.

Ma, C.K., Chang, J.M., Lin, D.C., 2003. Input forces estimation of beam structures by an inverse method. J. Sound Vib. 259, 387–407.

Macdonald, J.H., 2003. Evaluation of buffeting predictions of a cable-stayed bridge from full-scale measurements. J. Wind Eng. Ind. Aerodyn. 91, 1465–1483.

Maes, K., Lourens, E., Van Nimmen, K., Reynders, E., De Roeck, G., Lombaert, G., 2014. Design of sensor networks for instantaneous inversion of modally reduced order models in structural dynamics. Mech. Syst. Signal Process. 52, 628–644.

Maes, K., Gilljns, S., Lombaert, G., 2018. A smoothing algorithm for joint input-state estimation in structural dynamics. Mech. Syst. Signal Process. 98, 292–309.

Naets, F., Cuadrado, J., Desmet, W., 2015. Stable force identification in structural dynamics using Kalman filtering and dummy-measurements. Mech. Syst. Signal Process. 50, 235–248.

Niu, Y., Fritzen, C., Jung, H., Buethe, I., Ni, Y.-Q., Wang, Y.-W., 2015. Online simultaneous reconstruction of wind load and structural responses: theory and application to Canton tower. Comput. Aided Civ. Infrastruct. Eng. 30, 666–681.

Petersen, Ø.W., Øiseth, O., 2019. Finite element model updating of a long span suspension bridge. In: Rupakhety, R., Olafsson, S., Bessason, B. (Eds.), Proceedings of the International Conference on Earthquake Engineering and Structural Dynamics. Springer International Publishing, pp. 335–344.

Petersen, Ø.W., Øiseth, O., Lourens, E., 2019. Full-scale identification of the wave forces exerted on a floating bridge using inverse methods and directional wave spectrum estimation. Mech. Syst. Signal Process. 120, 708–726.

Qiao, B., Zhang, X., Gao, J., Chen, X., 2016. Impact-force sparse reconstruction from highly incomplete and inaccurate measurements. J. Sound Vib. 376, 72–94.

Rezayat, A., Nassiri, V., De Pauw, B., Ertveldt, J., Vanlanduit, S., Guillaume, P., 2016. Identification of dynamic forces using group-sparsity in frequency domain. Mech. Syst. Signal Process. 70, 756–768.

Scanlan, R., 1978. The action of flexible bridges under wind, II: buffeting theory. J. Sound Vib. 60, 201–211.

Scanlan, R., 1978. The action of flexible bridges under wind, I: flutter theory. J. Sound Vib. 60, 187–199.

Siedziako, B., Øiseth, O., Rønnquist, A., 2017. An enhanced forced vibration rig for wind tunnel testing of bridge deck section models in arbitrary motion. J. Wind Eng. Ind. Aerodyn. 164, 152–163.

Solari, G., De Gaetano, P., Repetto, M.P., 2015. Thunderstorm response spectrum: fundamentals and case study. J. Wind Eng. Ind. Aerodyn. 143, 62–77.

Song, W., 2018. Generalized minimum variance unbiased joint input-state estimation and its unscented scheme for dynamic systems with direct feedthrough. Mech. Syst. Signal Process. 99, 886–920.

Sun, H., Feng, D., Liu, Y., Feng, M.Q., 2015. Statistical regularization for identification of structural parameters and external loadings using state space models. Comput. Aided Civ. Infrastruct. Eng. 30, 843–858.

Wang, H., Hu, R., Xie, J., Tong, T., Li, A., 2012. Comparative study on buffeting performance of Sutong Bridge based on design and measured spectrum. J. Bridge Eng. 18, 587–600.

Wong, K., 2004. Instrumentation and health monitoring of cable-supported bridges. Struct. Control Health Monit. 11, 91–124.

Xu, Y., Chen, J., 2004. Characterizing nonstationary wind speed using empirical mode decomposition. J. Struct. Eng. 130, 912–920.

Zhi, L., Li, Q., Fang, M., 2016. Identification of wind loads and estimation of structural responses of super-tall buildings by an inverse method. Comput. Aided Civ. Infrastruct. Eng. 31, 966–982.

Zhi, L., Yu, P., Li, Q.-S., Chen, B., Fang, M., 2018. Identification of wind loads on super-tall buildings by Kalman filter. Comput. Struct. 208, 105–117.

Zhu, L., Xu, Y., Zhang, F., Xiang, H., 2002. Tsing Ma bridge deck under skew winds - Part I: aerodynamic coefficients. J. Wind Eng. Ind. Aerodyn. 90, 781–805.